JGR Space Physics

RESEARCH ARTICLE
10.1029/2020JA027877

Key Points:
- SABER data show that O number density between 95 and 100 km is higher in summer middle-high latitudes, opposite to the MSIS distribution
- The atomic oxygen distribution between 95 and 100 km affects the winds, temperature, composition and dynamics in the middle-upper thermosphere
- Correct lower thermospheric specification of atomic oxygen is important in modeling space weather and climate

Correspondence to:
G. Malhotra,
garimam@umich.edu

Citation:
Malhotra, G., Ridley, A. J., Marsh, D. R., Wu, C., Paxton, L. J., & Mlynczak, M. G. (2020). Impacts of lower thermospheric atomic oxygen on thermospheric dynamics and composition using the global ionosphere thermosphere model. *Journal of Geophysical Research: Space Physics*, *125*, e2020JA027877. https://doi.org/10.1029/2020JA027877

Received 3 FEB 2020
Accepted 31 JUL 2020
Accepted article online 21 AUG 2020

Impacts of Lower Thermospheric Atomic Oxygen on Thermospheric Dynamics and Composition Using the Global Ionosphere Thermosphere Model

Garima Malhotra[1], Aaron J. Ridley[1], Daniel R. Marsh[2], Chen Wu[1], Larry J. Paxton[3], and Martin G. Mlynczak[4]

[1]Climate and Space Sciences and Engineering, University of Michigan, Ann Arbor, MI, USA, [2]National Center for Atmospheric Research, Boulder, CO, USA, [3]Applied Physics Laboratory, Johns Hopkins University, Laurel, MD, USA, [4]NASA Langley Research Center, Hampton, VA, USA

Abstract The exchange of energy between the lower atmosphere and the ionosphere thermosphere system is not well understood. One of the parameters that is important in the lower thermosphere is atomic oxygen. It has recently been observed that atomic oxygen is higher in summer at ~95 km. In this study, we investigate the sensitivity of the upper thermosphere to lower thermospheric atomic oxygen using the Global Ionosphere Thermosphere Model (GITM). We use the Whole Atmosphere Community Climate Model with thermosphere and ionosphere extension (WACCM-X) to drive the lower atmospheric boundary of atomic oxygen in GITM between ~95 and 100 km and compare the results with the current mass spectrometer incoherent scatter (MSIS) driven GITM. MSIS has higher atomic oxygen in the winter hemisphere while WACCM-X has higher atomic oxygen in the summer hemisphere. The reversal of atomic oxygen distribution affects the pressure distribution between 100 and 120 km, such that the hemisphere with larger O number density has stronger equatorward winds, and lower temperature mainly due to adiabatic and radiative cooling. This affects thermospheric scale heights such that the hemisphere with more O has lower N_2 and thus enhanced O/N_2. This behavior is observed in the opposite hemisphere when MSIS is used as the lower boundary for GITM. Overall, O/N_2 for WACCM-X driven GITM matches better with the global ultraviolet imager (GUVI) data. We find that the impact of lower thermospheric atomic oxygen on upper thermosphere is not just through diffusive equilibrium but also through secondary effects on winds and temperature.

1. Introduction

The coupling between the lower atmosphere and the ionosphere-thermosphere (IT) system remains one of the biggest challenges in understanding and observing space weather. Numerous studies have been conducted over the past few decades to understand the dynamical and compositional changes in the IT densities and temperature because of the lower atmosphere (e.g., Hagan & Forbes, 2002; Immel et al., 2006; Malhotra et al., 2016; Shimazaki, 1967, 1968; X. Zhang et al., 2010b, 2010a, etc.). The vertical coupling via gravity waves, planetary waves, and atmospheric tides plays a crucial role in the momentum, energetics, and composition of the IT system (Lindzen, 1981; Qian et al., 2009; Siskind et al., 2014; Yamazaki & Richmond, 2013). Because most space-based activities are in the thermosphere/ionosphere of either Earth or other planets, it is imperative to understand the physical processes affecting this region of the atmosphere. For example, ionospheric irregularities impacting communication systems (e.g., Kelly et al., 2014), such as equatorial bubbles, are thought to be seeded from the lower and middle atmosphere (Hysell et al., 1990; Prakash, 1999; Rottger, 1973).

In order to better understand how the lower atmospheric variability at various spatial and temporal scales propagates into the upper atmosphere, attempts have been made to develop whole atmosphere models, such as, the Whole Atmosphere Community Climate Model with Thermosphere and Ionosphere Extension (WACCM-X) (H.-L. Liu et al., 2018), the Ground to topside model of Atmosphere and Ionosphere for Aeronomy (GAIA) (Jin et al., 2011), the Whole Atmosphere Model (WAM) (Akmaev et al., 2008; Fuller-Rowell et al., 2008), and the Canadian Middle Atmosphere Model (CMAM) (Beagley et al., 1997). Apart from

seamless atmospheric modeling, another approach to better understanding the lower atmospheric influences in the IT system is by coupling a lower atmosphere model with an IT/upper atmospheric model (e.g., Akmaev, 2011; Roble, 2013). While whole atmosphere models are more self-consistent, coupled models are better suited for isolating the effects of specific lower boundary conditions on the upper atmosphere (e.g., Hagan et al., 2009; Q. Wu et al., 2012).

For upper atmospheric models, lower boundary conditions are especially important for introducing compositional changes in the IT system, as the composition at 100–130 km map to higher altitudes because of diffusive equilibrium (Colegrove et al., 1966). Major constituents in the MLT are atomic oxygen (O), molecular nitrogen (N_2), and molecular oxygen (O_2). Between the altitudes 80 and 100 km, the lifetime of O changes from hours to several months, and therefore, O in the lower thermosphere becomes highly susceptible to dynamical transport by winds (Brasseur & Solomon, 1984; Smith et al., 2010). Changes in O concentration in this region map to total neutral densities at higher altitudes in the thermosphere as O becomes the major species above 200 km. It is also known that the electron density in the *F* region ionosphere is approximately proportional to O/N_2 because O acts as a source of free electrons while N_2 acts as the sink (Shimazaki, 1965, 1966).

In the upper thermosphere, a hemispheric asymmetry in the distribution of species is observed in solstice conditions. Higher concentrations of lighter species, for example, O and He are observed in the winter hemisphere, also called the "winter bulge," whereas heavier species (e.g., O_2 and N_2) are concentrated in the summer hemisphere (e.g., Johnson, 1964, 1973; Johnson & Gottlieb, 1970, 1973; Keating & Prior, 1968; King, 1964; Mayr et al., 1978; Reber et al., 1968). Two processes that are thought to be responsible for this redistribution are horizontal transport across the hemispheres and vertical transport. In the thermosphere, meridional wind circulation is dominated by interhemispheric winds from summer to winter due to the temperature gradient arising from asymmetrical solar heating between the hemispheres. Numerous studies (Cageao & Kerr, 1984; Mayr et al., 1978) have put forward the horizontal transport of O into the winter hemisphere by the meridional winds as the primary reason for the winter bulge. In the middle thermosphere, the vertical winds in the summer are largely upward whereas the vertical winds in the winter hemisphere are downward. This causes vertical transport of the species such that in the summer hemisphere, upward winds result in decrease of lighter species and increase of heavier species (Burns et al., 1989; Hays et al., 1973; Jones Jr. et al., 2018; X. Liu et al., 2014; Reber & Hays, 1973; Rishbeth, 1998). The opposite happens in the winter hemisphere resulting in a relative increase of lighter species and decrease of heavier species. The importance of one mechanism versus the other (i.e., horizontal vs. vertical transport) is still under investigation. Fuller-Rowell (1998) linked the two mechanisms by describing the mixing to be similar to a huge eddy, calling it the "thermospheric spoon." Sutton (2016) found that both phenomena are inherently linked with one another with convergent horizontal motion increasing downwelling and divergent motion increasing upwelling, thereby transporting light constituents both horizontally and vertically simultaneously.

In the mesosphere, the meridional circulation is in the same direction, from summer to winter, but driven by a different mechanism. Large westward gravity wave drag in the winter hemisphere, and eastward gravity wave drag in the summer hemisphere causes the circulation to be from summer to winter through Coriolis force (Qian & Yue, 2017). Smith et al. (2010) used O mixing ratio at 0.0046 hPa (~84 km) from the Sounding of the Atmosphere using Broadband Emission Radiometry (SABER) instrument to show that there is a winter maximum in O which is likely linked to the abovementioned gravity wave driven downwelling in the winter. However, they observed the opposite hemispheric distribution at a lower pressure, 0.0008 hPa (~94 km) with higher O mixing ratio in the summer hemisphere and lower in the winter hemisphere. The greatest variation was found to be at midlatitudes with the phase of midlatitude variation reversing between 84 and 94 km. The level of reversal was found to be at 0.001 hPa (~93 km). The higher summer atomic oxygen concentration may be an indication that the summer upwelling circulation cell has reversed and there is a downward circulation cell above the mesopause (~83–89 km) (Smith et al., 2010). Another reason may be enhanced molecular diffusion of O due to higher temperatures from higher altitudes (Smith et al., 2010). A similar reversal was also observed by Russell et al. (2004) using Wind Imaging Interferometer (WINDII) data and Sheese et al. (2011) using Optical Spectrograph and Infrared Imaging System (OSIRIS) data. Qian et al. (2017) found evidence of lower thermospheric winter to summer circulation using WACCM-X and SABER CO_2 data citing convergence in summer and divergence in winter about 10 km above the mesopause. It was explained to be forced by gravity waves (Lindzen, 1981; H.-L. Liu, 2007; Rezac et al., 2015; Smith et al., 2011). It is possible that this circulation is responsible for the distribution of

atomic oxygen observed by Smith et al. (2010). Qian and Yue (2017) studied the impact of the lower thermospheric winter-to-summer circulation on the upper thermosphere by forcing the meridional and vertical winds of the NCAR Thermosphere-Ionosphere-Electrodynamics General Circulation Model (TIE-GCM) (Qian et al., 2014; Richmond et al., 1992, and references therein) in the altitude range of ~97–110 km toward a winter-to-summer circulation. They found that upwelling decreases the upper thermospheric O/N_2 in the winter hemisphere, whereas, downwelling increases it in the summer hemisphere, thus reducing the gradient between the two hemispheres.

This study reports the impact of changing the distribution of the lower thermospheric atomic oxygen on the upper thermosphere. This is done by changing the lower boundary condition for atomic oxygen in the Global Ionosphere Thermosphere Model (GITM) from an empirical model (mass spectrometer incoherent scatter, MSIS) to a whole atmosphere model (WACCM-X). MSIS and WACCM-X have oppositely oriented atomic oxygen distributions in latitude, with WACCM-X having a distribution that is more consistent with observations. This is done while keeping other species' number densities, temperature, and winds constant at the model lower boundary. This is different from Qian and Yue (2017) because our goal is to explain the mechanisms that are involved in lower-upper thermospheric coupling in the context of lower thermospheric O concentration rather than the winter-to-summer circulation.

2. Methodology

2.1. Models

2.1.1. GITM

GITM is a physics-based three-dimensional spherical model that simulates the thermosphere and ionosphere by determining the density, momentum, and energy self-consistently (Ridley et al., 2006). GITM explicitly solves for the neutral densities of O, O_2, $N(^2D)$, $N(^2P)$, $N(^4S)$, N_2, NO, and He; and ion species $O^+(^4S)$, $O^+(^2D)$, $O^+(^2P)$, O_2^+, N^+,N_2^+, NO^+, and He^+. It uses a stretched altitude grid from 100 to 600 km that allows for nonhydrostatic conditions to exist (Deng et al., 2008). The vertical grid spacing is less than 3 km in the lower thermosphere and over 10 km in the upper thermosphere. It allows different models of high-latitude electric fields, auroral particle precipitation, and solar EUV inputs to be used. Here, we use the Weimer model (Weimer, 2005) for the high-latitude potential, FISM EUV empirical model (Chamberlin et al., 2008), and NOAA POES Hemispheric Power-driven model (Fuller-Rowell & Evans, 1987) as an estimate of power deposited in the polar regions by energetic particles.

2.1.2. MSIS Radar

In its default configuration, GITM uses the MSIS radar model, NRLMSISE-00 (Hedin, 1983, 1987, 1991; Picone et al., 2002) as the thermospheric lower boundary condition on the number densities and temperature. NRLMSISE-00 is an empirical model that uses Fourier-modulated spherical harmonics in latitude, longitude, and time, and Bates-Walker (Walker, 1965) and cubic spline fits in the vertical to numerous satellite, ground based and rocket observations. NRLMSISE-00 has been widely used to understand vertical coupling between the lower atmosphere and the IT system (Fuller-Rowell, 1998; H.-L. Liu et al., 2010; Qian et al., 2018; Weimer et al., 2018; Yue et al., 2019). Since it is an empirical model, it gives a good estimate of neutral densities and temperature for average conditions where observations exist. The inputs to MSIS are the solar flux proxy, F10.7, and geomagnetic activity level (Ap).

2.1.3. WACCM-X

WACCM-X is also a physics-based model, covering the whole atmosphere starting from the surface to 2.5×10^{-9} hPa or ~500 km in altitude (H.-L. Liu et al., 2010, 2018). It is based on the NCAR WACCM (Garcia et al., 2007; Marsh et al., 2013), which in turn is based on the NCAR Community Atmosphere Model (CAM) (Lin, 2004). In this study, we use the specified dynamics configuration of WACCM-X, also known as SD-WACCM-X. In this configuration, dynamical fields (temperature, zonal and meridional winds, and surface pressure) are specified in the troposphere and stratosphere from the Modern Era Retrospective Analysis for Research and Applications (MERRA) (Rienecker et al., 2011). WACCM-X can also be run without constraining the troposphere and stratosphere, also usually referred to as the free-running mode. Since we are only using the results from SD-WACCM-X here, we will refer to these simulations as WACCM-X. The horizontal resolution (latitude × longitude) of the model is 1.9° × 2.5°, and the time step is 5 min. A detailed description of WACCM-X is given in H.-L. Liu et al. (2010) and H.-L. Liu et al. (2018). Hourly averaged values are used in our study. WACCM-X is used as the lower boundary for GITM and the simulation

Table 1
Parameter Values at the Lower Boundary—GITM w/ MSIS and GITM w/ WACCM-X

Parameter	Value
Temperature, T	150 K
Zonal winds, U	0 m/s
Meridional winds, V	0 m/s
Molecular oxygen, O_2	1×10^{18} m^{-3}
Molecular nitrogen, N_2	1×10^{19} m^{-3}
Nitric oxide, NO	1×10^{14} m^{-3}

results are compared with MSIS-driven GITM. The version of Community Earth System Model (CESM) that is used in this study is 2.0.

WACCM-X solves the Navier-Stokes equations in pressure coordinates, whereas GITM solves them in altitude coordinates. WACCM-X outputs the mixing ratio for different species, whereas GITM uses number densities as boundary conditions. Therefore, the total neutral number density in WACCM-X is calculated from pressure and temperature fields (using the ideal gas law). WACCM-X also outputs the altitude corresponding to each pressure level at every grid cell. The total number densities and atomic oxygen mixing ratio in pressure coordinates are converted to altitude coordinates by linearly interpolating them to 95, 97.5, and 100 km, thus putting them on a uniform altitude grid. The total number density is multiplied by the mixing ratio of atomic oxygen (also in altitude coordinates) to get number densities for atomic oxygen on the altitude grid.

2.2. GITM Simulations

Atomic oxygen number densities from MSIS and WACCM-X were used as inputs at the lower boundary of GITM. WACCM-X is expected to have significantly more variability owing to nonmigrating tides, planetary waves and gravity waves that propagate through the lower atmosphere to the thermosphere. On the other hand, because MSIS is an empirical model, it should provide a good estimate of average conditions but may not be as accurate in representing the impact of forcing from above (e.g., magnetospheric inputs) or forcing from below (e.g., atmospheric gravity waves). Also, at these altitudes, MSIS has only the mean component and migrating tides with a small dependence on F10.7 and Ap. It should be noted that real time-varying geospace conditions are used as inputs in these simulations.

To specify the lower boundary condition in GITM, two ghost cells below 100 km are used. In these cells, state values are specified. In order to not drive constant acceleration, a hydrostatic solution is used, where the density is set in the cell closest to 100 km (second cell), and the density in the lower cell is derived. In both the simulations, the temperature in both cells and across the globe were held constant at 150 K, while all components of the winds were held to be zero. For O_2, N_2, and NO, the number densities in the second cell are constant across the globe and specified in Table 1. For the minor species, He and N(^{4}S), MSIS is used to specify the number densities in both the simulations. For O, a zero gradient in altitude is used since O peaks in this region. Therefore, the O number densities in the first cell are same as in the second cell. O is allowed to have horizontal structure, such that, for the GITM w/ MSIS simulation, MSIS is used to specify the O number densities, whereas, for the GITM w/ WACCM-X simulation, the abovementioned linearly interpolated O number densities are used.

Hourly averaged WACCM-X O number densities are used. Since the time steps in GITM are much smaller than the 1 hr time resolution of WACCM-X output, WACCM-X number densities are linearly interpolated in time between every hour. These number densities are linearly interpolated to GITM's second cell's altitude and grid locations. MSIS O number density is computed at each GITM time step and location. The only difference between the two runs, GITM w/ MSIS and GITM w/ WACCM-X is the atomic oxygen between 95 and 100 km. This was specifically done to explore the effect of the O number density in the lower thermosphere on the system.

Results from the two simulations spanning 21 days, 15 January 2010 to 4 February 2010 are discussed here. Since, it took around 9 days for the model to achieve a nearly steady globally averaged O density at 200 km altitude, results from the last 12 days, 24 January 2010 to 4 February 2010 are discussed. The two simulations are referred to as GITM w/ MSIS and GITM w/ WACCM-X. This time period is chosen because it is a geomagnetically quiet time around solstice that results in a hemispherically asymmetric lower thermospheric O number density between MSIS and WACCM-X. Simulations results from 24 June 24, 2010 to 5 July 2010 are also discussed here.

2.3. Data

In this study, SABER data are used to validate the lower thermospheric atomic oxygen in WACCM-X. We also use Global Ultraviolet Imager (GUVI) O/N_2 to validate the integrated thermospheric O/N_2 in GITM once

the lower boundary atomic oxygen is changed from MSIS to WACCM-X. A brief description of the SABER and GUVI instruments is provided below for the interested reader.

2.3.1. SABER

Sounding of the Atmosphere using Broadband Emission Radiometry (SABER) is an instrument on Thermosphere-Ionosphere-Mesosphere Energetics and Dynamics (TIMED) satellite. Its primary goal is to quantify the energy budget of mesosphere and lower thermospheric (MLT) (Mlynczak, 1996, 1997). TIMED was launched in 2001 in a 74.1° inclination orbit at an altitude of 630 km (Russell III et al., 1999; Yee, 2003). It has a yaw period of ~60 days in which the latitudinal coverage alternates between 82°N to 53°S and 53°N to 82°S. SABER has a vertical resolution of ~2 km and horizontal resolution of ~300 km depending on the limb geometry. SABER takes limb scan profiles of 10 spectral channels between 1.27 and 17 μm, indicating the kinetic temperature of O and CO_2 in the MLT region (~65–105 km) (Rezac et al., 2015).

O is generated by photodissociation of molecular oxygen by solar UV radiation and has two very bright fine structure lines, 63.184 μm (4.75 THz) and 145.525 μm (2.06 THz). However, both of these wavelengths are particularly hard to measure with the current state-of-the-art satellites instruments. Past and present technologies require a detection system cooled to cryogenic 4 K temperatures, which poses a significant mission cost and lifetime overhead. D. L. Wu et al. (2016) described an emerging technique, THz limb sounder (TLS) using a Schottky-diode-based receiver which has good radiometric sensitivity at noncryogenic temperature. Studies over the last few decades have used balloons (Lin et al., 1987; Mlynczak et al., 2004), rocket borne in situ observations (Gumbel, 1997; K. Grossmann & Offermann, 1978; Offermann, 1974; von Zahn, 1967) and space station observations (K. U. Grossmann et al., 2000). Since there are no global observations made by observing radiant emission of O directly, SABER calculates O using indirect methods (Mlynczak, 1996, 1997; Rezac et al., 2015). During the daytime, O is derived using the emission of ozone (O_3) at 9.6 μm assuming that there is an equilibrium between the photolysis of O_3 and the recombination of O and O_2. During night, it is inferred from the emission of the vibrationally excited Meinel OH band, which is formed by the reaction between atomic hydrogen (H) and O_3. This measurement assumes that there is an equilibrium between this reaction and the recombination of O and O_2 (Mlynczak et al., 2013, 2018).

2.3.2. GUVI

The GUVI is a far ultraviolet hyperspectral imager aboard the TIMED satellite, measuring the terrestrial airglow from 120 to 180 nm (Christensen et al., 2003). Some of the objectives of GUVI are to make accurate observations of thermospheric temperature and composition and to understand the response of thermosphere ionosphere system to various energy fluxes. It measures in five far ultraviolet bands corresponding to emission features of H (121.6), OI (130.4), OI (135.6), and the N_2 Lyman-Birge-Hopfield (LBH) bands (Christensen et al., 1994, 2003; Paxton et al., 1999). In the imaging mode, a scan mirror subsystem (Humm et al., 1998, 1999) scans the instantaneous field of view cross-track of the satellite once every 15 s. The scan begins on the limb and covers 140°, that is, 80° from nadir above the limb on the cold side of the satellite (away from the Sun) to 60° toward the warm side (Paxton et al., 2004). Since December 2007 when the scan mirror failed, GUVI only operates in the spectral stare mode at about 47° from nadir. In this mode, data are recorded continuously from all 176 spectral pixels for each of the 14 spatial pixels (Meier et al., 2014). The height-integrated O/N_2 ratio referenced at a N_2 column-integrated number density of 10^{17} cm^{-2} is obtained from the disk 135.6 nm and LBHS day glow data (Y. Zhang et al., 2004, 2014).

3. Results and Discussion

3.1. Lower Boundary Comparison

Figure 1 shows a comparison between atomic oxygen number densities of GITM w/ MSIS (Figure 1a) and GITM w/ WACCM-X (Figure 1b) at 100 km, averaged over the last 12 days of the simulation. For GITM w/ MSIS, O is higher in the northern winter whereas for GITM w/ WACCM-X, O is higher in the southern summer. Figure 1c shows the difference between panels (b) and (a), that is, GITM w/ WACCM-X - GITM w/ MSIS. The absolute difference is larger in the summer hemisphere.

In order to determine which simulation result is closer to the observed O distribution, Figure 2a shows SABER atomic oxygen number densities at 100 km gridded in 4° × 4° bins, averaged for January from 2002–2017. Figure 2b shows the number of measurements in each bin. The high latitudes have lower numbers of measurements compared to middle-lower latitudes, because of the inclination of TIMED satellite. Long-term averaging is helpful in reducing the uncertainty associated with the decrease in abundance of

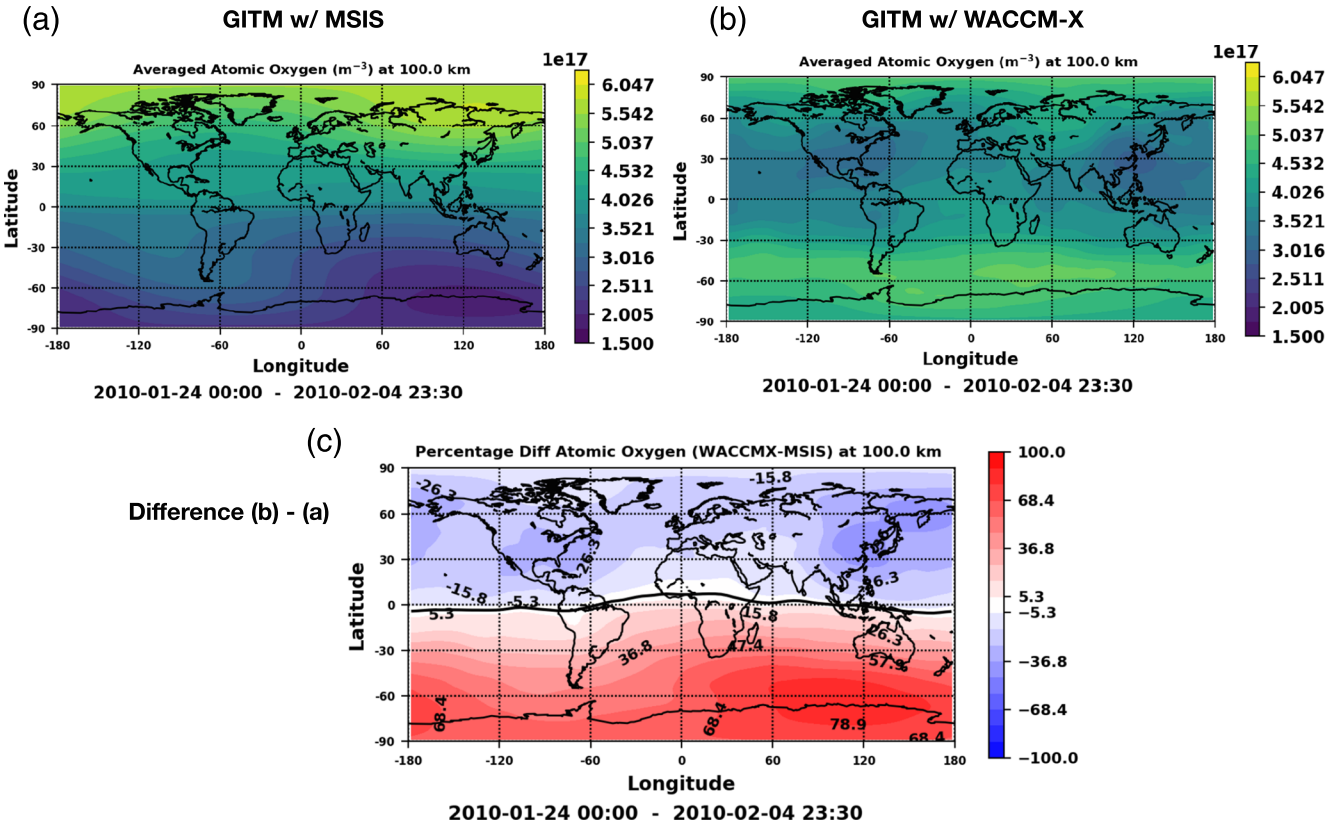

Figure 1. (a) Atomic oxygen for GITM w/ MSIS at 100 km averaged for time periods 24 January 2010 to 4 February 2010. (b) Similar to (a) but for GITM w/ WACCM-X. (c) Averaged difference in atomic oxygen at 100 km: GITM w/ WACCM-X (b)—GITM w/ MSIS (a). Note the thicker black line roughly parallel to the equator. This is the zero line where no difference is seen.

daytime ozone due to photolysis. The atomic oxygen number densities are larger in the summer (Southern) Hemisphere which is similar to Figure 1b for GITM w/ WACCM-X. The summer hemisphere number density maximum is at different latitudes, with the SABER maximum occurring at higher latitudes than the WACCM-X maximum. Because of the lower number of SABER measurements at high summer latitudes, there is a greater statistical uncertainty associated with the measurements. Another source of uncertainty is the accuracy of the temperature at 100 km, through the recombination rate coefficient in the steady-state chemical expression used to derive atomic oxygen from ozone (Mlynczak et al., 2013). Lastly, SABER daytime ozone has a likely high bias as reported by Smith et al. (2013). Thus, the absolute magnitude of SABER data is different from both MSIS and WACCM-X. SABER values are ~3 times the model values, resulting in a larger gradient between the hemispheres. Using WACCM-X O number densities as an approximation for the true O number density distribution, this study focuses on explaining the large-scale effects of the O number density distribution at the mesopause on the thermosphere.

As an aside, MSIS was developed using data from a wide variety of in situ satellite measurements in the upper themosphere (Hedin, 1987, 1991; Picone et al., 2002) and did not include measurements of O in this region. At around 100 km, a hemispheric gradient in the atomic oxygen number density in MSIS is predicted, with lower O number density in the summer hemisphere, similar to the observations in the middle-upper thermosphere (Reber & Hays, 1973). However, in the region between 90 and 150 km, limited observations were available, primarily being temperature and total neutral density measurements inferred from rockets and incoherent scatter radars. NRLMSISE-00 did not include the SABER measurements in its fitting procedure because TIMED hadn't been launched yet. In MSIS, below the turbopause (~105 km), the number densities were extrapolated using the average molecular weight of the atmosphere assuming a perfectly mixed atmosphere along with a correction factor to account for chemical and dynamical flow effects on various species. Below the turbopause, these chemical dynamical correction factors imply that the atmosphere is not fully mixed until ~80 km or lower. Between 120 and 105 km, the number densities are a meld of their

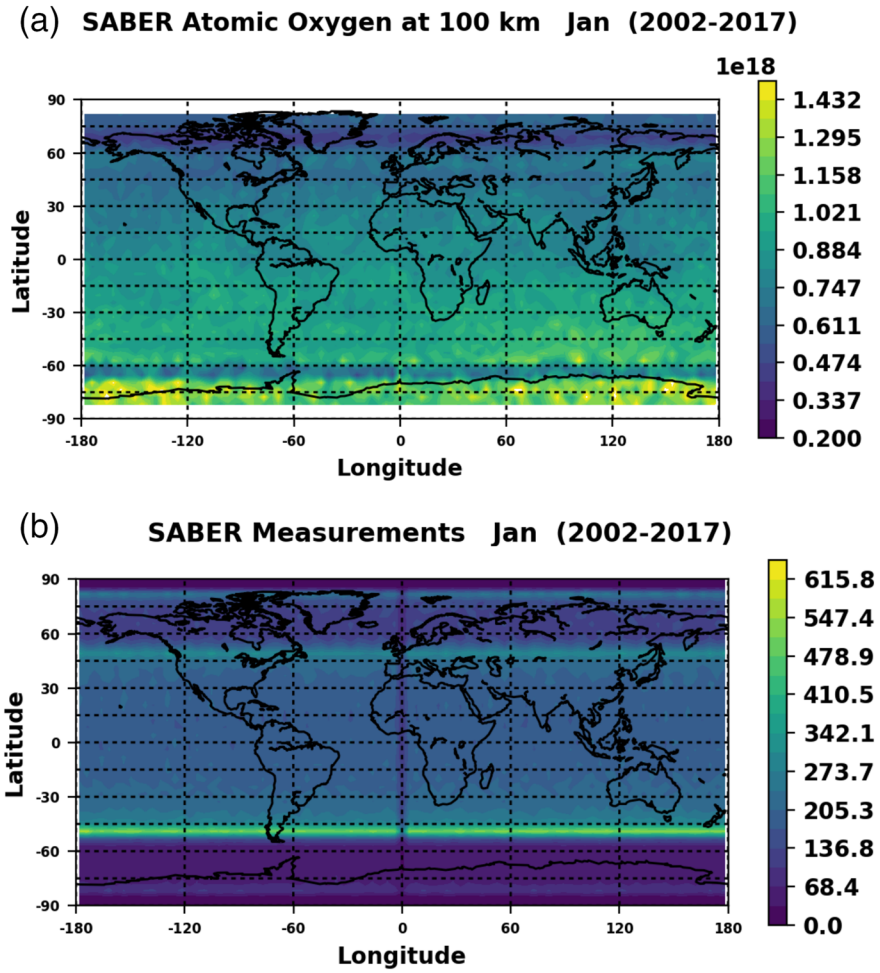

Figure 2. (a) Atomic oxygen for SABER in number m^{-3} at 100 km for the month of January binned together for the years 2002–2017. The bin size is 4° × 4°. (b) Number of measurements in each bin for the month of January for 2002–2017.

fully mixed and diffusively separated values along with the correction factor. The correction factor for O does not take into account the dynamical/chemical effects that lead to larger summer atomic oxygen, thus explaining the similar hemispheric gradient of atomic oxygen number density in the upper as well as the lower thermosphere.

However, O departs from diffusive and fully mixed equilibrium in the mesosphere and lower thermosphere due to chemistry, eddy mixing, and dynamic transport, which is highlighted by the incorrect O distribution in MSIS, as compared to both WACCM-X results and SABER observations. One of the reasons for the O reversal in SABER data is suggested by Smith et al. (2010) through the effect of temperature and molecular diffusion. Higher temperatures in the summer hemisphere may lead to molecular diffusion of O from higher to lower altitudes resulting in high O concentration. The transport of O via lower thermosphere winter to summer circulation suggested by Qian and Yue (2017) and Rezac et al. (2015) may also be the reason for this reversal. Another contribution to high summer O can be from the eddy turbulence or eddy diffusion. Eddy diffusion is a macroscopic description of flow induced by the gravity wave motion (Hodges, 1969). However, previous studies suggest that other tidal and wave activity can contribute to the mixing and turbulence in this region (Jones Jr. et al., 2017; Salinas et al., 2016). Numerous observational (e.g., Fukao et al., 1994; Kirchhoff & Clemesha, 1983; Sasi & Vijayan, 2001) and modeling studies (e.g., Pilinski & Crowley, 2015; Qian et al., 2009; Salinas et al., 2016) have found that eddy diffusion coefficient is larger in summer and smaller in winter. However, the exact magnitude of the eddy diffusion term near the turbopause still remains elusive. We have yet to achieve a universal model for specifying the eddy diffusion coefficient. It is possible

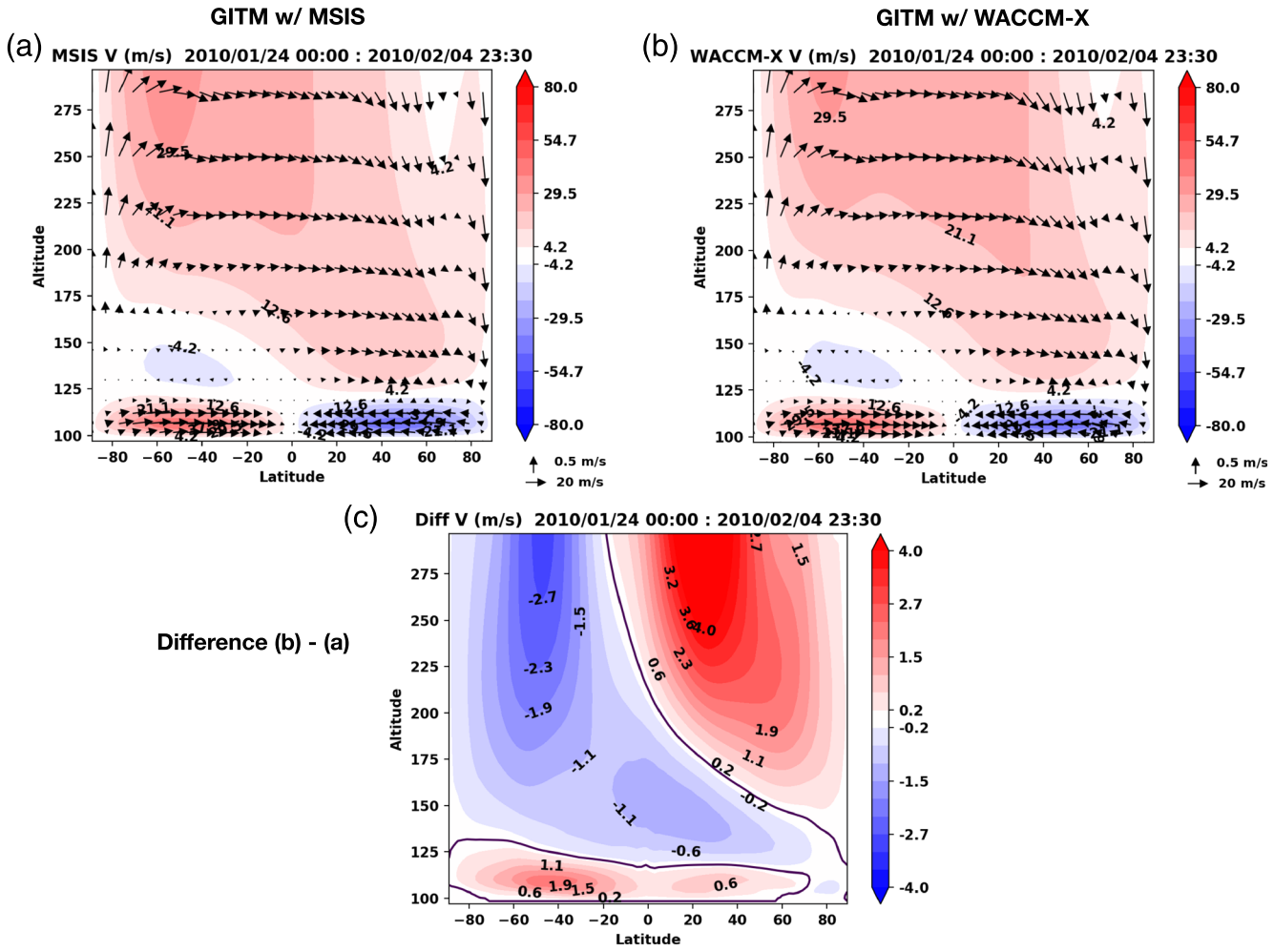

Figure 3. (a) The contours indicate the zonally averaged meridional wind in m/s for GITM w/ MSIS averaged for 24 January 2010 to 4 February 2010. Positive values indicate northward wind while negative values indicate southward wind. The arrows signify a vector sum of meridional and vertical winds (scaled by ×50). (b) Similar to (a) but for GITM w/ WACCM-X. (c) Averaged difference in meridional winds, GITM w/ WACCM-X (b)—GITM w/ MSIS (a). Note the thicker black contour line. This is the zero line where no difference is seen.

that larger eddy diffusion during summer leads to downward transport of O into the lower thermosphere resulting in the increase of summer O/N_2.

3.2. Effect on Lower-Upper Thermosphere

Figure 3 shows GITM zonally averaged meridional winds in the thermosphere from 100 to 275 km. Figures 3a and 3b are the winds for GITM w/ MSIS and GITM w/ WACCM-X, respectively. Winds vectors comprising of both vertical (scaled by 50) and meridional winds components are overlaid on the contour plots. The general circulation remains similar between the two simulations. Between 100 and 120 km, winds are equatorward and above 160 km the circulation is dominated by summer to winter winds with upwelling in summer and downwelling in winter at middle-high latitudes.

Figure 3c is the difference between the zonally averaged meridional winds, GITM w/ WACCM-X - GITM w/ MSIS. As mentioned previously, the only difference between the two simulations is the atomic oxygen distribution below 100 km. The difference in Figure 3c is positive in the region between 100 and 120 km. This indicates that GITM w/ WACCM-X has larger equatorward winds in the summer (Southern) Hemisphere, whereas GITM w/ MSIS has larger equatorward winds in the winter (Northern) Hemisphere. This is because of the difference in latitudinal O number density gradient between the two simulations such that, the winds induced by the lower boundary O gradient superimpose on the main equatorward circulation cells. Thus, because of the opposite O distribution, the hemisphere with larger equatorward winds simply reverses.

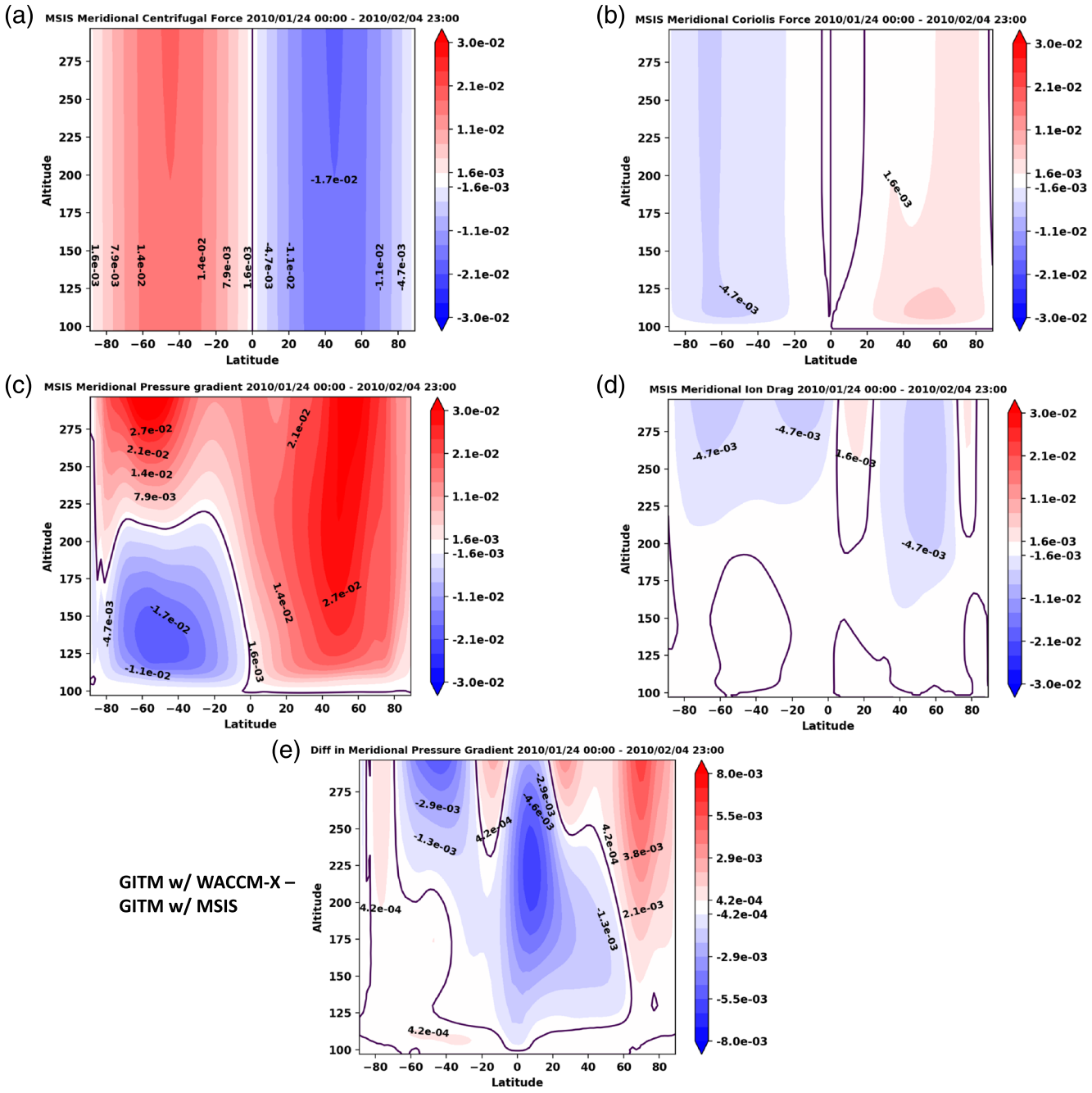

Figure 4. (a) The contours indicate the force terms of northward momentum equation in m/s^2 for GITM w/ MSIS, zonally averaged for 24 January 2010 to 4 February 2010. (b) Similar to (a) but for Coriolis force. (c) Similar to (a) but for pressure gradient force. Positive values indicate that the pressure is increasing from north to south. (d) Similar to (a) but for Ion Drag. (e) Averaged difference in meridional pressure gradient forces, GITM w/ WACCM-X—GITM w/ MSIS. Note the thicker black contour line. This is the zero line where no difference is seen.

The forces affecting the winds in the thermosphere can be understood by investigating the contribution of force terms of the horizontal momentum equation. The northward momentum equation in GITM is as follows (Ridley et al., 2006):

$$\frac{\partial u_\theta}{\partial t} = -u_r \frac{\partial u_\theta}{\partial r}^{(1)} - \frac{u_\theta}{r}\frac{\partial u_\theta}{\partial \theta}^{(2)} - \frac{u_\phi}{r\cos\theta}\frac{\partial u_\theta}{\partial \phi}^{(3)} - \frac{k_b}{\overline{m_n} r}\frac{\partial T}{\partial \theta}^{(4)} - \frac{T}{r\rho}\frac{k_b}{\overline{m_n}}\frac{\partial \rho}{\partial \theta}^{(5)} + \frac{\mathcal{F}_\theta}{\rho}^{(6)} - \frac{{u_\phi}^2 \tan\theta}{r}^{(7)} - \frac{u_\theta u_r}{r}^{(8)} - \Omega^2 r\cos\theta\sin\theta^{(9)} - 2\Omega u_\phi \sin\theta^{(10)} \quad (1)$$

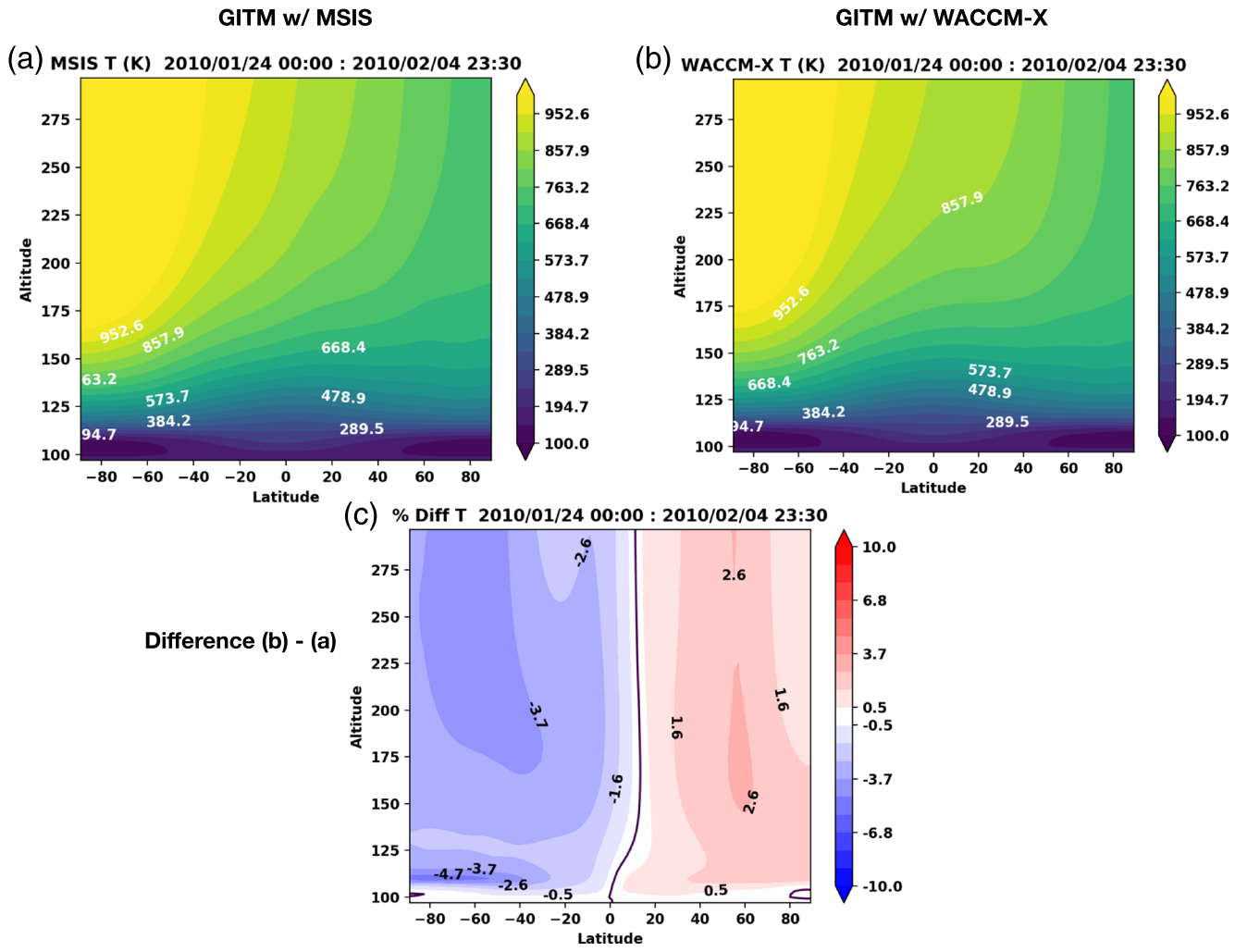

Figure 5. (a) The contours indicate the temperature in K for GITM w/ MSIS zonally averaged for 24 January 2010 to 4 February 2010. (b) Similar to (a) but for GITM w/ WACCM-X. (c) Zonally averaged percentage difference in temperatures GITM w/ WACCM-X (b)—GITM w/ MSIS (a). Note the thicker black contour line. This is the zero line where no difference is seen.

where θ denotes the north latitude, ϕ denotes east longitude, r is the radial distance from the center of the Earth, u is the neutral velocity, Ω is the angular velocity of the planet, k_b is the Boltzmann constant, m_n is the number density weighted average mass, T is the neutral temperature, and ρ is the mass density. $\mathcal{F}_\theta$ is the force due to ion-neutral friction and viscosity in θ direction. The superscript for each term is for notation purposes only. Terms (1), (2), and (3) on the right represent the advective terms from the total derivative of velocity. Terms (7) and (8) are the velocity terms due to the spherical coordinates. Terms (4) and (5) represent the force arising from pressure gradient. Terms (9) and (10) are the centrifugal and Coriolis force terms, respectively.

Figure 4 shows the zonally and temporally averaged centrifugal (Figure 4a), Coriolis (Figure 4b), pressure gradient (Figure 4c), and ion drag (Figure 4d) forces from GITM w/ MSIS. It should be noted that these figures represent the force terms on the right side of Equation 1 with the appropriate sign. Clearly, on average, the centrifugal and pressure gradient forces dominate this region of the thermosphere. Below 120 km, near the boundary of the model, the pressure gradient force in Figure 4c is weak owing to a nearly constant boundary condition on number densities (except O), temperatures, and winds. Thus, the two equatorward circulation cells between 100 and 120 km are driven by centrifugal force shown in Figure 4a. In the middle thermosphere, between 125 and 200 km, the winds can develop creating a pressure bulge and can cause a redistribution of the temperature and densities to create oppositely directed forces that cancel

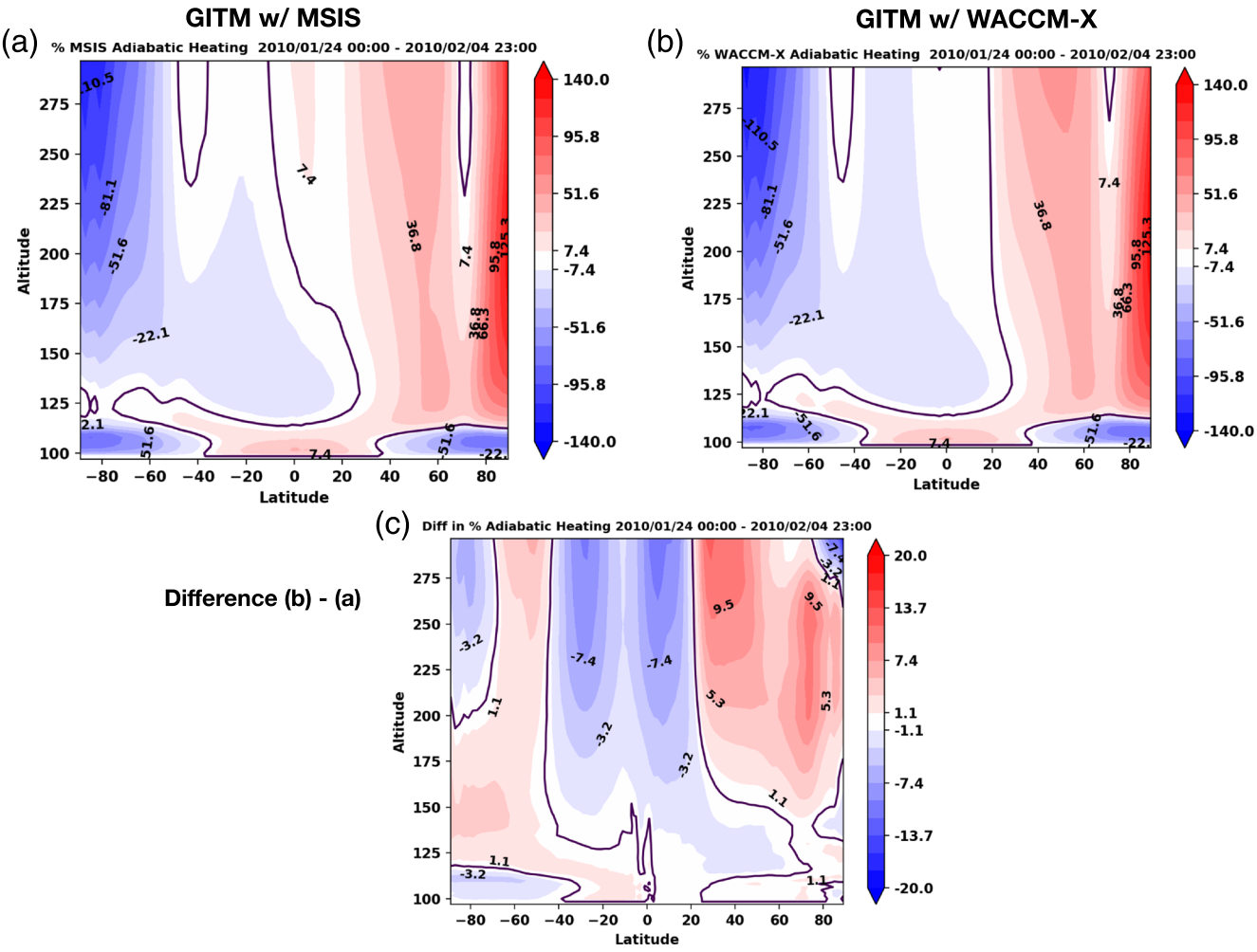

Figure 6. (a) The contours indicate the percent adiabatic heating per day (normalized by temperature) for GITM w/ MSIS zonally averaged for 24 January 2010—4 February 2010. (b) Similar to (a) but for GITM w/ WACCM-X. (c) Zonally averaged difference in adiabatic heating GITM w/ WACCM-X (b)—GITM w/ MSIS (a). Note the thicker black contour line. This is the zero line where no difference is seen.

the centrifugal force. A more-precise boundary condition on the pressure would have a bulge at the equator, such that the latitudinal gradient in pressure more closely balances the centrifugal force (i.e., an oblate-spheroid atmosphere instead of a perfect sphere). We refer to this as the poleward directed pressure gradient force. Above this altitude range, the pressure gradient force is from the summer to winter because of the temperature gradient, driving the main circulation. Coriolis force shown in Figure 4b is weak and acts opposite to the centrifugal force. Ion drag shown in Figure 4b is also weak and has a significant magnitude only above 200 km, where it acts mostly against the main circulation.

Figure 4e shows the difference between the pressure gradient forces of GITM w/ WACCM-X and GITM w/ MSIS. The differences corresponding to other force terms are negligible and are not shown here. Between 100 and 120 km, a small difference exists between the simulations which can be largely attributed to the density gradient difference. This difference results in the wind differences shown in Figure 3c. GITM w/ WACCM-X (GITM w/ MSIS) has weaker pressure gradient force in the summer (winter) hemisphere. More O at summer high latitudes in GITM w/ WACCM-X weakens the poleward directed pressure gradient force which increases the acceleration due to centrifugal force, resulting in stronger winds as compared to GITM w/ MSIS. Similarly, GITM w/ MSIS has weaker poleward directed pressure gradient force and larger acceleration due to centrifugal force in the winter hemisphere. The wind difference between 140 and 200 km altitude will be discussed later. It is important to note that the change in lower boundary O only changes

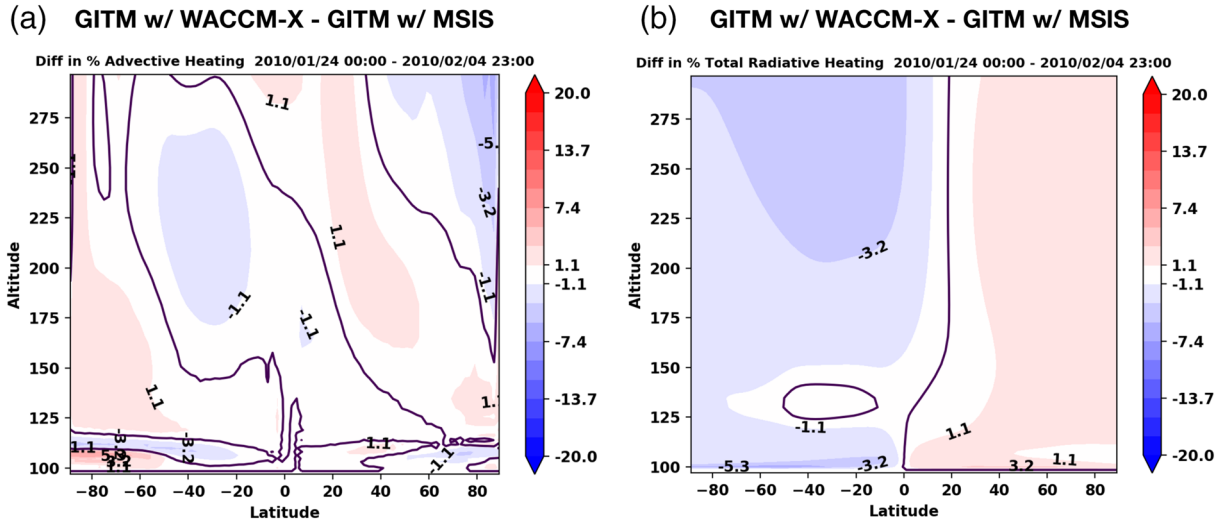

Figure 7. (a) The contours indicate the difference in percent advective heating per day (normalized by temperature), GITM w/ WACCM-X—GITM w/ MSIS, zonally averaged for 24 January 2010 to 4 February 2010. (b) Similar to (a) but for radiative heating. Note the thicker black contour line. This is the zero line where no difference is seen.

the magnitude of the winds and does not change the direction of the wind. The transition to the upper thermospheric summer to winter circulation starts above 120 km, resulting in high atomic oxygen in the winter hemisphere above this altitude in both the simulations. This was also observed by K. U. Grossmann et al. (2000) at an altitude of 140 km using CRISTA experiments.

Figure 5 shows the zonally averaged temperature for the two simulations. Figures 5a and 5b are the temperature plots for GITM w/ MSIS and GITM w/ WACCM-X, respectively, while Figure 5c is the percent difference between the two. The temperature shows a similar pattern between Figures 5a and 5b. The temperatures are the lowest in the high-latitude region in the 100–120 km altitude range. This can be attributed to the adiabatic and advective cooling due to the equatorward circulation cells as shown previously in Figure 3. Above this altitude, there is a sharp increase in the temperature with temperatures rising up to 1,000 K in summer (Southern) Hemisphere. As seen in Figure 5c, the temperature difference between the two simulations starts at altitudes slightly above 100 km. In the summer hemisphere, GITM w/ WACCM-X has a lower temperature, while in the winter hemisphere, GITM w/ MSIS has a lower temperature. The temperature difference is as high as 5% (35 K) in the Southern Hemisphere. Thus, reversing the O number density distribution at the lower boundary leads to a change in lower thermospheric temperature, that is, lower thermospheric temperatures occur at latitudes with higher O concentrations.

Figures 6a and 6b show the zonally averaged percent adiabatic heating per day (normalized by temperature) for GITM w/ MSIS and GITM w/ WACCM-X, respectively. For both the simulations the overall heating pattern remains similar. In the lower thermosphere, between 100 and 120 km, the high latitudes have adiabatic cooling, and the lower latitudes have adiabatic heating. The reason for this is the equatorward wind cells as mentioned before and shown in Figure 3. Above 125 km, the summer hemisphere experiences adiabatic cooling (due to diverging winds), and the winter hemisphere gets warmer (due to converging winds) because of the summer to winter circulation. The difference between the two simulations is shown in Figure 6c. Between 100 and 120 km, in the summer hemisphere, GITM w/ WACCM-X has more adiabatic cooling because of larger equatorward winds. Similarly, in the winter hemisphere, GITM w/ MSIS has a tiny bit more adiabatic cooling. Above this altitude region, the adiabatic heating difference shows a roughly similar pattern as the wind difference of Figure 3c. In the summer hemisphere, except at middle-high latitudes, GITM w/ WACCM-X has more adiabatic cooling while in the winter hemisphere, GITM w/ MSIS has more adiabatic cooling. It should be noted that adiabatic heating differences in Figure 6c do not exactly

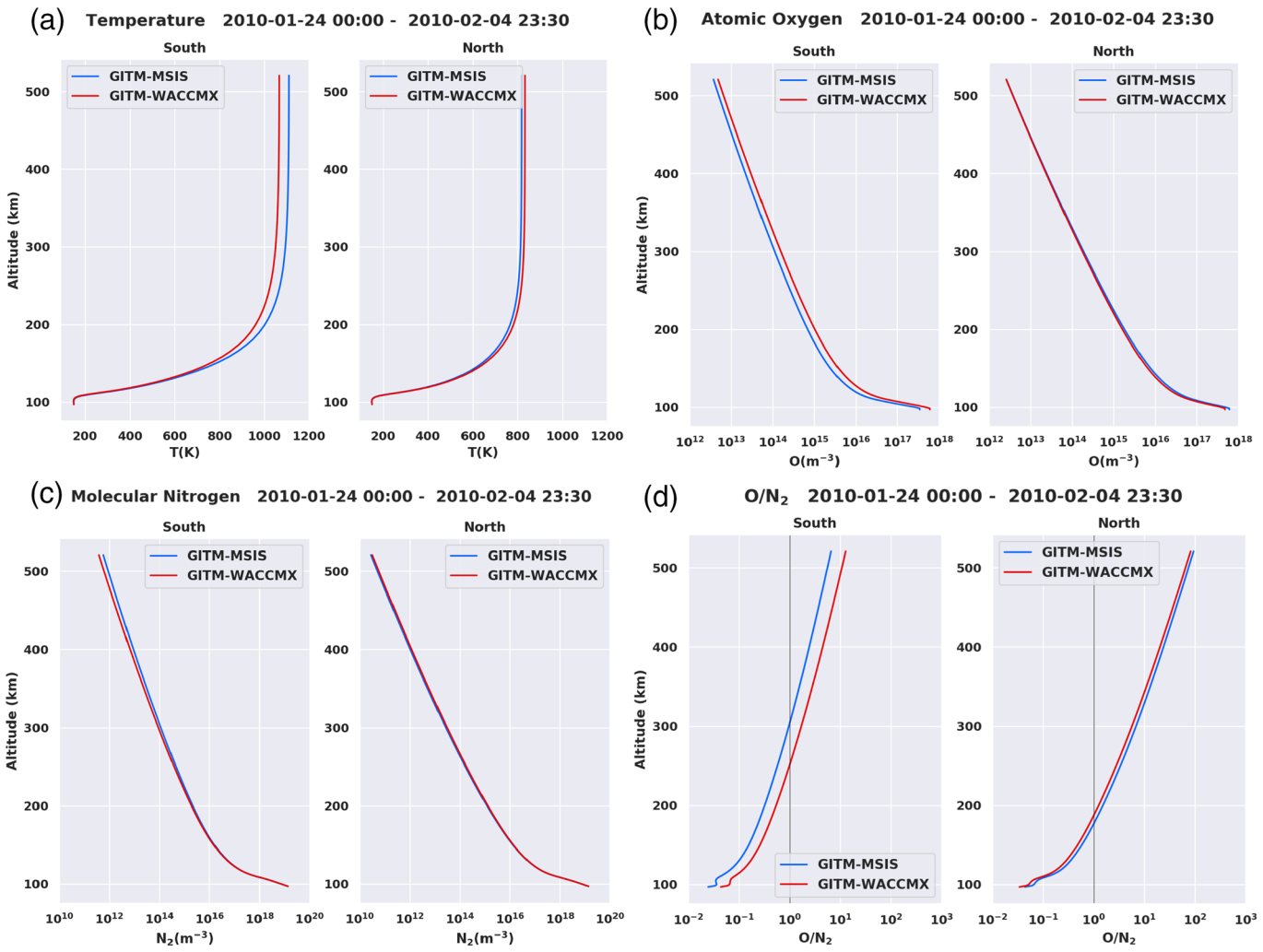

Figure 8. Height profile for (a) temperature (K), (b) atomic oxygen (m^{-3}), (c) molecular nitrogen (m^{-3}), (d) O/N_2 averaged for 24 January 2010 to 4 February 2010. The *x* axis indicates the values of each parameter while *y* axis is the altitude. The red (blue) curves are for GITM w/ WACCM-X (MSIS). Each parameter is divided into Northern and Southern Hemispheres, and cosine-weighted averaged for latitudes 30–90°. The black vertical line in (d) indicates where O/N_2 is 1.

correspond to the temperature difference of Figure 5c. This is because of the contribution of other terms of the energy equation.

Figures 7a and 7b show the percent difference between the two simulations for advective and radiative heating per day (normalized by temperature), respectively. For both GITM w/ MSIS and GITM w/ WACCM-X, advective heating shows similar heating patterns (not shown here), and largely follows the meridional wind patterns of Figure 3. Meridional winds in the upper thermosphere advect fluid parcels of higher temperature from summer to winter, resulting in heating in the winter hemisphere, whereas equatorward winds in the lower thermosphere advect fluid parcels of lower temperature from higher latitudes, resulting in cooling at lower latitudes. The difference between the two simulations as shown in Figure 7a is small relative to the adiabatic heating differences and largely follows the meridional wind differences at midlatitudes of Figure 3. The radiative cooling comes from a combination of CO_2 cooling in the 100–120 km altitude range, NO cooling in the 100–150 km range and O cooling above that. In the summer hemisphere, GITM w/ WACCM-X has larger O and therefore, less total radiative heating (more cooling), and in the winter hemisphere, GITM w/ MSIS has larger O and thus less radiative heating. The sum of these three terms, Figures 6c, 7a, and 7b largely explains the temperature difference observed in Figure 5c, as the radiative heating mostly

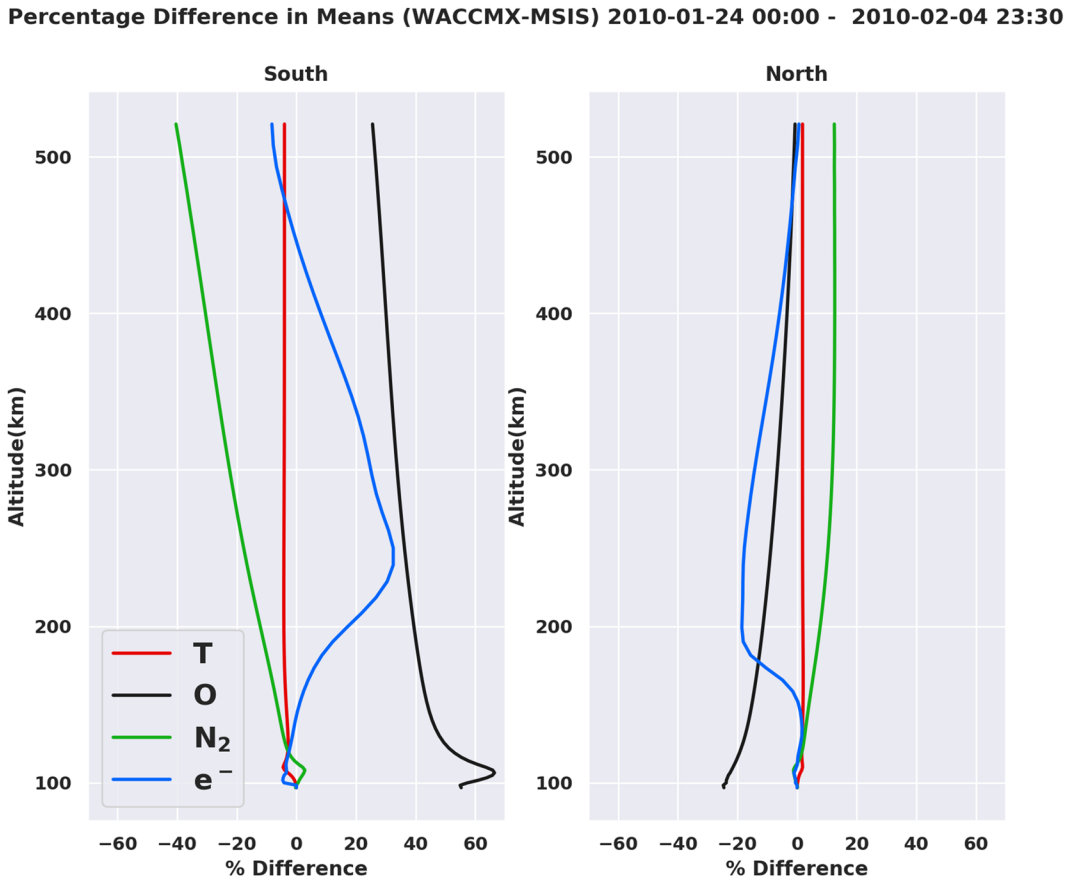

Figure 9. Height profile for the percentage difference in GITM w/ WACCM-X—GITM w/ MSIS for temperature (red), O (black), N_2 (green), electron density (blue). These profiles are averaged for 24 January 2010 to 4 February 2010 and cosine-weighted averaged for latitudes 30–90° and divided into Northern and Southern Hemispheres.

compensates for the anomalous differences (e.g., GITM w/ MSIS has larger adiabatic cooling in summer middle-high latitudes) in Figure 6c. The contribution of other terms of the energy equation are analyzed as well (not shown here): (a) The difference between the two simulations for auroral heating is negligible in comparison to the abovementioned terms, (b) chemical heating difference has a significant magnitude and reinforces the temperature differences in Figure 5c, (c) the molecular conduction heating and Joule heating differences have an opposite distribution as the other terms and mainly contribute in reducing the magnitude of the overall heating difference. The sum of these individual heating terms do not exactly correspond to the temperature distribution of Figure 5c, indicating the nonlinearity of the thermospheric dynamics.

Figure 8 shows the mean height profiles of temperature, O, N_2, and O/N_2 separated into Northern and Southern Hemispheres averaged poleward of ±30° latitude. The red and blue curves are for GITM w/ WACCM-X and GITM w/ MSIS simulations, respectively. Larger differences between the curves exist in the summer (Southern) Hemisphere for all parameters. Figure 9 shows the percentage difference between the two simulations for temperature, O, N_2, and the electron density. Figures 8a and 9 show that the difference in temperature between the two simulations remains roughly constant with altitude. The effect of the change in temperature on neutral number densities can be understood using diffusive equilibrium as a rough guide (e.g., Schunk & Nagy, 2009).

$$n_s(z) = n_s(z_o) \times \frac{T_s(z_o)}{T_s(z)} \times e^{-\int_{z_o}^{z} \frac{(dz')}{H_s}}, \tag{2}$$

$$H_s = \frac{k_B T_s}{m_s g} \tag{3}$$

where $n_s(z)$ and $T_s(z)$ are the number density and temperature at altitude z, respectively. The parameters $n_s(z_o)$ and $T_s(z_o)$ are the number density and temperature at a reference altitude z_o, respectively. H_s is the

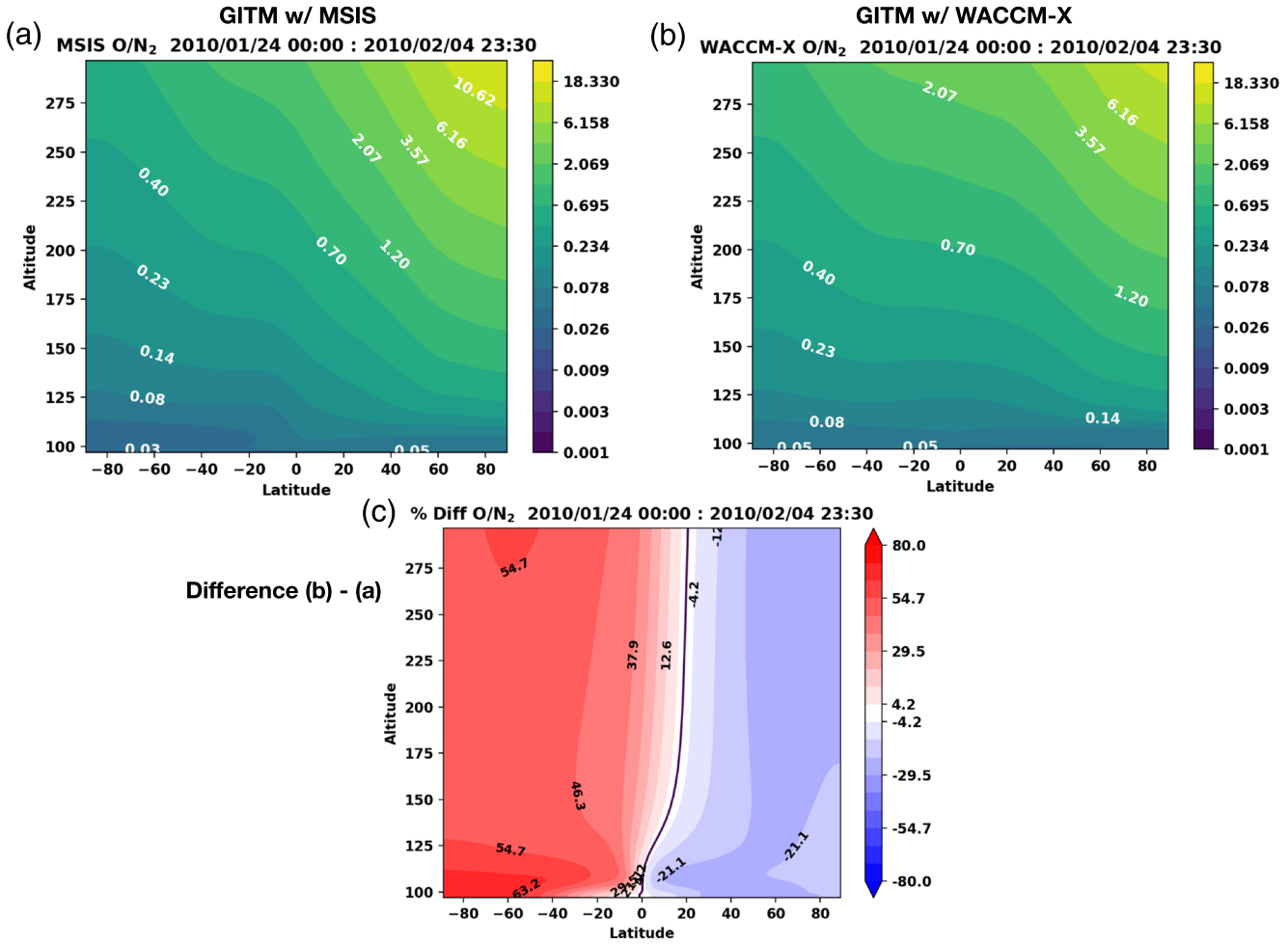

Figure 10. (a) The contours indicate the O/N_2 for GITM w/ MSIS averaged for 24 January 2010 to 4 February 2010 using a logarithmic color scale. (b) Similar to (a) but for GITM w/ WACCM-X. (c) Averaged difference in O/N_2 GITM w/ WACCM-X (b)—GITM w/ MSIS (a). Note the thicker black contour line. This is the zero line where no difference is seen.

scale height for each species and is directly proportional to temperature, T_s and inversely proportional to the mass of the species, m_s. k_B is the Boltzmann constant and g is the acceleration due to gravity. We can break Equation 2 into two contributing terms, the temperature ratio term, $\frac{T_s(z_o)}{T_s(z)}$, and the scale height term, $e^{-\int_{z_o}^{z}\frac{(dz')}{H_s}}$ (This is just for nomenclature; the scale height term depends on temperature, too).

For N_2 (assuming z_o to be at 100 km), number densities are the same between the two simulations at 100 km ($n_s(z_o)$) and the entire difference arises because of different distributions of O at the boundary. The temperature at the lower boundary ($T_s(z_o)$) is also the same between the simulations. In the Southern Hemisphere, GITM w/ WACCM-X has lower temperature ($T_s(z)$) (Figure 5) resulting in larger temperature ratio term, causing an increase in N_2 number densities. Whereas, the scale height term is smaller causing a decrease in N_2 number densities. The effect of these two terms cancel each other and as a result, the difference in N_2 number densities between the two simulations is small in the lower thermosphere. In the upper thermosphere, the difference in the temperature ratio terms between the simulations remains the same, while the difference in the scale height terms becomes larger because of the integrated effect of exponential. As a result, N_2 decreases faster for GITM w/ WACCM-X in the Southern Hemisphere, because of lower temperature and smaller scale height. Therefore, the difference in N_2 between the two simulations increases with height as seen in Figure 9. The percentage difference of N_2 reaches about ~10% in the Northern Hemisphere and ~−30% in the Southern Hemisphere.

For the atomic oxygen profile in Figure 8b, the lower boundary number density term ($n_s(z_o)$) is important because the two simulations have different O at the lower boundary. The difference is as large as ~50%

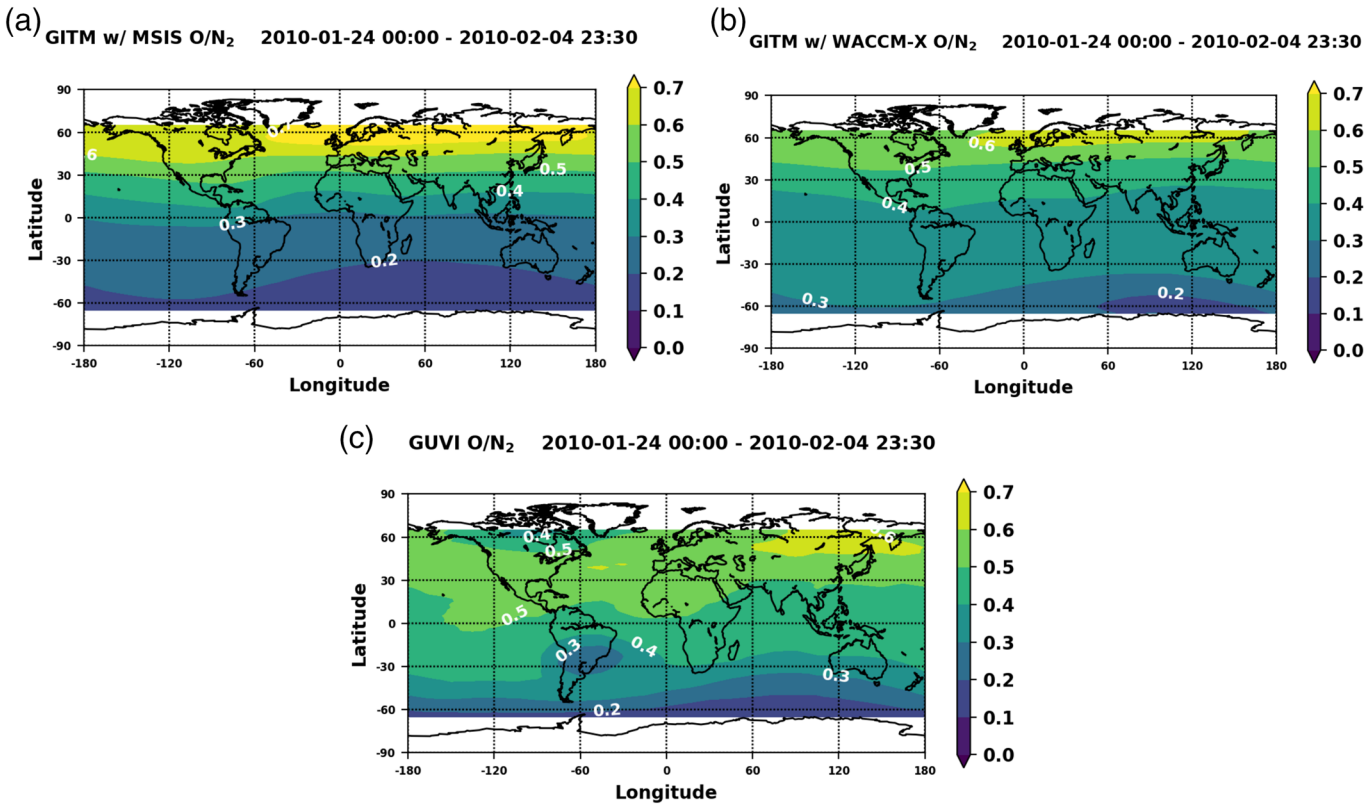

Figure 11. Integrated O/N_2 with a reference altitude of 10^{17} cm^{-2} for (a) GITM w/ MSIS, (b) GITM w/ WACCM-X, (c) TIMED GUVI data. The O/N_2 in GITM are sampled at GUVI times and locations.

at 100 km as seen in Figure 9. Moreover, the contribution of the temperature ratio term reinforces the difference in $n_s(z_o)$ between the two simulations. In the lower thermosphere, at southern latitudes, GITM w/ WACCM-X has larger $n_s(z_o)$ and larger temperature ratio term because of the lower temperature, which results in increased O. However, in the upper thermosphere, as the scale height term becomes important, a lower temperature and thus a lower scale height has the opposite effect on O as it acts to decrease the O number densities faster (also observed for N_2 above). Similarly, GITM w/ MSIS has higher temperature in this hemisphere resulting in larger scale height and a slower decrease. Therefore, the difference between the simulations reduces in magnitude with altitude in Figure 9. For the Northern Hemisphere, the difference between $n_s(z_o) \times \frac{T_s(z_o)}{T_s(z)}$ at lower altitudes is small as also shown in Figure 1. In the lower thermosphere, this term dominates. However, with increasing altitude, the effect of scale height causes the O number densities for the two simulations to become very close in magnitude and eventually at higher altitudes causes the difference to reverse. It should also be noted that the lower thermosphere is dominated by dynamics and the diffusive equilibrium reasoning here is used as a rough guide to understand the vertical profiles of different species.

Figure 8d shows the height profiles for O/N_2. O/N_2 increases with altitude due to larger rate of decrease of N_2 as compared to O (N_2 has smaller scale height because of its larger mass). In the Southern Hemisphere, GITM w/ WACCM-X has larger O and smaller N_2 resulting in larger O/N_2 which affects the electron density. In the Northern Hemisphere, the situation is reversed where GITM w/ MSIS has larger O/N_2 and electron density. Figure 9 also shows the percentage difference in height profile of electron density between the two simulations. The difference ranges between 10% and 40% at F region altitudes and follows the O/N_2 difference in both the hemispheres.

Contour plots for O/N_2 are shown in Figure 10. Above ~120 km, both simulations show similar patterns in O/N_2 with larger values in the winter hemisphere. This is indicative of the summer to winter circulation shown in Figure 3. Figure 10c shows the percent difference between the two simulations. The difference is as large as 60% between the two simulations in the lower thermosphere in the Southern Hemisphere. The

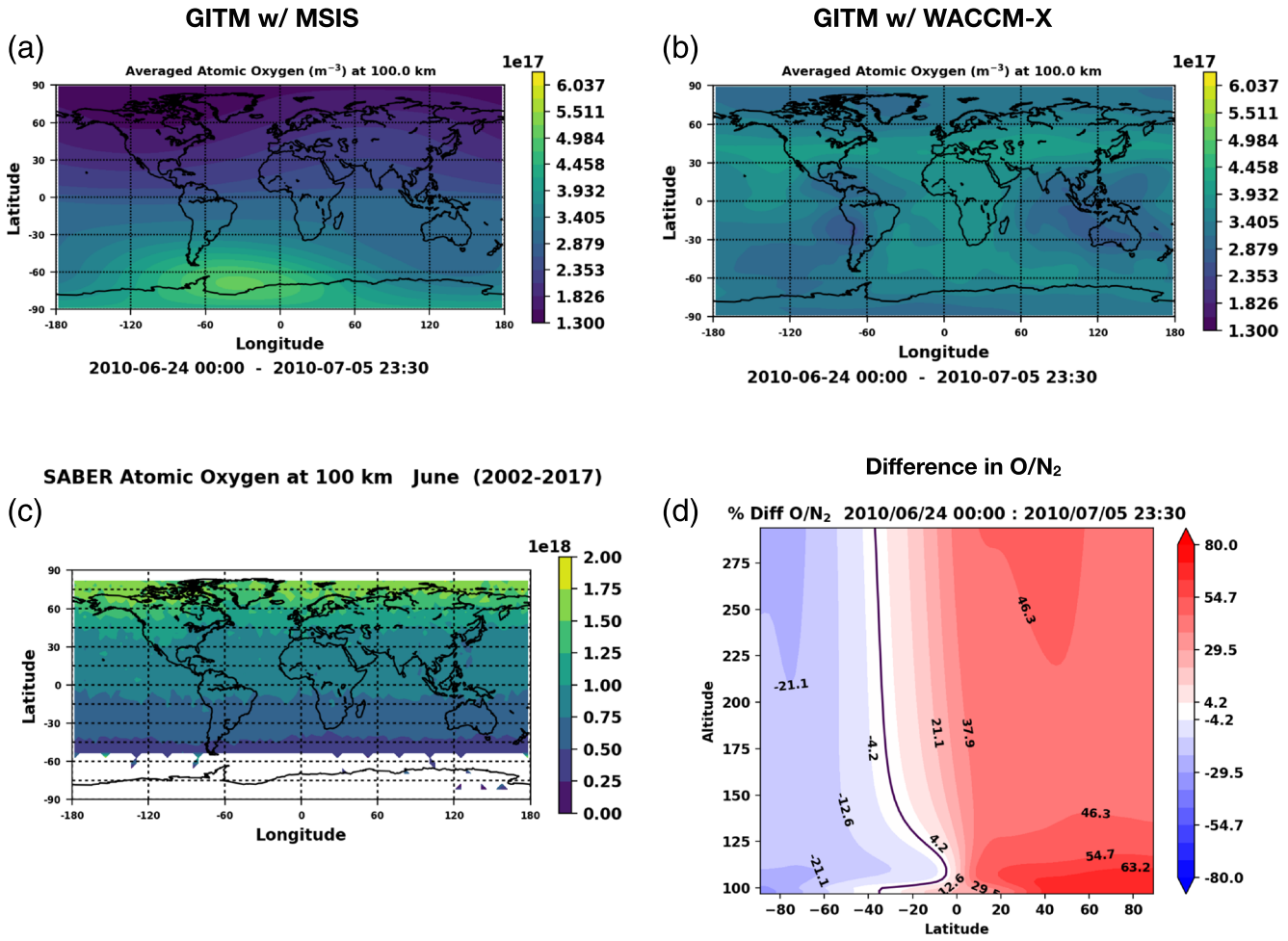

Figure 12. Atomic oxygen (m^{-3}) at 100 km averaged from 24 June 2010 to 5 July 2010 for (a) GITM w/ MSIS, (b) GITM w/ WACCM-X. (c) Atomic oxygen for SABER in m^{-3} interpolated at 100 km for the month of January binned together for the years 2002–2017. The bin size is 4° × 4°. (d) Averaged difference in O/N_2 GITM w/ WACCM-X—GITM w/ MSIS for 24 June 2010 to 5 July 2010. Note the thicker black contour line. This is the zero line where no difference is seen.

effect of lower thermospheric O distribution superimposes on the overall O/N_2 distribution in the upper thermosphere, leading to increases in O/N_2 in the hemisphere with larger lower thermospheric O. The effect of using O number densities from WACCM-X is to decrease the overall O/N_2 gradient between the two hemispheres. This result is similar to that observed by Qian and Yue (2017). When comparing the global averages, GITM w/ WACCM-X has higher O/N_2, resulting in larger electron density.

Above 125 km, as shown in Figure 3, the winds are dominated by northward interhemispheric winds. Figure 3c showed that the winds in the upper thermosphere are slower for GITM w/ WACCM-X in the Southern Hemisphere and faster in the Northern Hemisphere. From Figure 10c, GITM w/ WACCM-X has ~20–30% more O/N_2 than GITM w/ MSIS in the equatorial region. This mainly comes from +~20% in O and −~10% difference in N_2. It can be observed from Figure 4e that GITM w/ WACCM-X has smaller northward directed pressure gradient in most of the summer and winter hemisphere at midlatitudes and larger at higher latitudes in the winter hemisphere. The latitudinal gradient of higher equatorial O in GITM w/ WACCM-X leads to slower northward winds in the summer hemisphere and faster northward winds in the winter hemisphere as compared to GITM w/ MSIS which has higher winter O. This change in interhemispheric winds is in equilibrium with the reduced O/N_2 gradient for GITM w/ WACCM-X. Because the thermosphere is a nonlinear system, changes in densities, temperatures, and winds further affect the transport and density distribution. Only the first-order impact of lower thermospheric O distribution on the upper thermosphere is considered here.

Figure 11 shows a comparison between integrated O/N_2 for the two simulations and GUVI observations. As mentioned previously, using GITM w/ WACCM-X decreases the gradient in O/N_2 between the two hemispheres. Figure 11 shows O/N_2 is higher for GITM w/ WACCM-X in the Southern Hemisphere and lower in the Northern Hemisphere as compared to GITM w/ MSIS. In both hemispheres, GITM w/ WACCM-X matches with GUVI observations (Figure 11c) better. We would expect the correction of N_2 and other parameters in the lower thermosphere to bring the model results even closer to the observations. It was shown by Perlongo et al. (2018) that GITM has lower summer electron densities than the GPS TEC observations in both the northern and southern midlatitudes. Using GITM w/ WACCM-X at the lower boundary, this will potentially be corrected as the electron density depends on the O/N_2.

When the opposite solstice (i.e., June) is considered, the opposite behavior is observed. Figure 12 shows atomic oxygen distributions and O/N_2 for the month of June. GITM w/ WACCM-X and SABER number densities are similar in O distribution, although they are off in magnitude, while the MSIS-driven simulation has the opposite gradient in O. Figure 12d shows the height profile of difference in O/N_2 between the two simulations. This is opposite of Figure 10c. Thus, the opposite O distribution in the lower thermosphere affects both solstices in a similar, but opposite, way.

As mentioned above, the decrease in O/N_2 gradient in GITM w/ WACCM-X is consistent with the results obtained by Qian and Yue (2017). They explained the mechanism via vertical mixing due to lower thermospheric winter to summer circulation but did not show the species distribution in the lower thermosphere as a result of this circulation. Whereas this work starts with the species distribution in the lower thermosphere to observe the impact on the upper thermosphere. It is found that the O distribution at the mesopause affects the upper thermosphere in a more direct way than just through molecular diffusion: it impacts the wind and temperature distributions which subsequently changes the scale heights of molecular species. It is also found that using this distribution increases the global O/N_2 which is opposite to the result obtained by Qian and Yue (2017). However, this difference depends on the lower thermospheric species distribution from WACCM-X in our study and thus will change depending on the variability of the phenomena leading to this distribution.

4. Conclusions

Variations in O in the mesosphere and the lower thermosphere affect the composition and dynamics of the upper thermosphere as it becomes a major species above 200 km. Previous studies (Rezac et al., 2015; Russell et al., 2004; Smith et al., 2010) have shown that the summer hemisphere has higher atomic oxygen concentration in the lower thermosphere (90–100 km). Qian et al. (2017) suggested that the lower thermosphere winter to summer circulation is responsible for the high summer concentration of CO_2 in this region. In this study, we investigate the effect of the MLT O distribution on the composition and dynamics of the middle-upper thermosphere using an ionosphere-thermosphere model, GITM. Conventionally, GITM uses O distribution that is higher in winter from MSIS at its lower boundary. We change the lower boundary O distribution to be higher in summer, as specified by WACCM-X, which also matches better with the observations from SABER. We find that the reversal of O hemispheric concentration changes the magnitudes of the winds between 100 and 120 km due to the differences in pressure gradients. The hemisphere with larger O number densities has larger equatorward winds resulting in adiabatic cooling in that hemisphere. Larger radiative cooling in that hemisphere also leads to the cooling of that hemisphere. Other terms of the temperature equation such as advective, chemical, auroral, Joule, and molecular conduction heating also change and affect the temperature distribution. Overall, the lower temperature decreases the scale height of N_2 and other molecular species in the hemisphere with more lower thermospheric O, resulting in a reduction of their number densities at higher altitudes. We also find that the averaged O densities at 100 km in both MSIS and WACCM-X are much lower than SABER. If these O densities would have been much closer to SABER, we would expect higher O in the thermosphere in both the simulations. We would also expect a net lower temperature in the thermosphere due to larger radiative cooling, which would then also change the wind magnitudes.

In January, the Southern Hemisphere has larger atomic oxygen in GITM w/ WACCM-X (and SABER data) as compared to GITM w/ MSIS, larger equatorward winds, more adiabatic and radiative cooling, lower temperature, and lower N_2. This results in an increased O/N_2 and electron densities in the Southern (summer) Hemisphere in the GITM w/ WACCM-X simulation. The opposite behavior is observed in the Northern

(winter) Hemisphere. The change in O/N_2 is as large as 63% in the summer hemisphere in the lower thermosphere. This also slows down the northward interhemispheric winds in the summer hemisphere and speeds them up in the winter hemisphere. It is found that the vertical column integrated O/N_2 in GITM w/ WACCM-X matches the TIMED GUVI O/N_2 measurements better in both the hemispheres, as GITM w/ MSIS tends to understimate O/N_2 in the summer and overestimate it in the winter hemisphere. We would expect the correction of other mesopause boundary drivers within GITM such as N_2 and temperature to further improve the agreement between model results and the observations.

Data Availability Statement

The atomic oxygen used in this study is from SABER data Version 2.0 and was downloaded from this site (http://saber.gats-inc.com/data.php). The level 3 O/N_2 GUVI data was downloaded from this site (http://guvitimed.jhuapl.edu/). The GITM runs that were used in this study can be accessed at this site (https://doi.org/10.7302/yagm-xv95).

Acknowledgments
This work was supported by DoD GrantFA9550-16-1-0071. High computing resources were provided through Pleiades supercomputer by NASA Advanced Supercomputing (NAS) housed at NASA Ames Research Center and through Cheyenne supercomputer (https://doi.org/10.5065/D6RX99HX) by NCAR's Computational and Information Systems Laboratory sponsored by the National Science Foundation and other agencies.

References

Akmaev, R. A. (2011). Whole atmosphere modeling: Connecting terrestrial and space weather. *Reviews of Geophysics*, *49*, RG4004. https://doi.org/10.1029/2011RG000364

Akmaev, R. A., Fuller-Rowell, T. J., Wu, F., Forbes, J. M., Zhang, X., Anghel, A. F., et al. (2008). Tidal variability in the lower thermosphere: Comparison of whole atmosphere model (WAM) simulations with observations from TIMED. *Geophysical Research Letters*, *35*, L03810. https://doi.org/10.1029/2007GL032584

Beagley, S. R., de Grandpé, J., Koshyk, J. N., McFarlane, N. A., & Shepherd, T. G. (1997). Radiative dynamical climatology of the first generation Canadian middle atmosphere model. *Atmosphere-Ocean*, *35*(3), 293–331. https://doi.org/10.1080/07055900.1997.9649595

Brasseur, G., & Solomon, S. (1984). *Aeronomy of the middle atmosphere* (pp. 201–319). Dordrecht, Holland: D. Reidel Pub. Co.

Burns, A. G., Killeen, T. L., & Roble, R. G. (1989). Processes responsible for the compositional structure of the thermosphere. *Journal of Geophysical Research*, *94*(A4), 3670–3686. https://doi.org/10.1029/JA094iA04p03670

Cageao, R., & Kerr, R. (1984). Global distribution of helium in the upper atmosphere during solar minimum. *Planetary and Space Science*, *32*(12), 1523–1529. https://doi.org/10.1016/0032-0633(84)90019-9

Chamberlin, P. C., Woods, T. N., & Eparvier, F. G. (2008). Flare irradiance spectral model (FISM): Flare component algorithms and results. *Space Weather*, *6*, S05001. https://doi.org/10.1029/2007SW000372

Christensen, A. B., Paxton, L. J., Avery, S., Craven, J., Crowley, G., Humm, D. C., et al. (2003). Initial observations with the global ultraviolet imager (GUVI) in the NASA TIMED satellite mission. *Journal of Geophysical Research*, *108*(A12), 1451. https://doi.org/10.1029/2003JA009918

Christensen, A. B., Walterscheid, R. L., Ross, M. N., Meng, C.-I., Paxton, L. J. Jr., Anderson, D. E., et al. (1994). Global ultraviolet imager (GUVI) for the NASA Thermosphere-Ionsphere-Mesosphere Energetics and Dynamics (TIMED) mission. In J. Wang & P. B. Hays (Eds.), *Optical spectroscopic techniques and instrumentation for atmospheric and space research* (Vol. 2266, pp. 451–466). Bellingham, Wash: International Society for Optics and Photonics. https://doi.org/10.1117/12.187583

Colegrove, F. D., Johnson, F. S., & Hanson, W. B. (1966). Atmospheric composition in the lower thermosphere. *Journal of Geophysical Research*, *71*(9), 2227–2236. https://doi.org/10.1029/JZ071i009p02227

Deng, Y., Richmond, A. D., Ridley, A. J., & Liu, H.-L. (2008). Assessment of the non-hydrostatic effect on the upper atmosphere using a general circulation model (GCM). *Geophysical Research Letters*, *35*, L01104. https://doi.org/10.1029/2007GL032182

Fukao, S., Yamanaka, M. D., Ao, N., Hocking, W. K., Sato, T., Yamamoto, M., et al. (1994). Seasonal variability of vertical eddy diffusivity in the middle atmosphere: 1. Three year observations by the middle and upper atmosphere radar. *Journal of Geophysical Research*, *99*(D9), 18,973–18,987. https://doi.org/10.1029/94JD00911

Fuller-Rowell, T. J. (1998). The "thermospheric spoon": A mechanism for the semiannual density variation. *Journal of Geophysical Research*, *103*(A3), 3951–3956. https://doi.org/10.1029/97JA03335

Fuller-Rowell, T. J., Akmaev, R. A., Wu, F., Anghel, A., Maruyama, N., Anderson, D. N., et al. (2008). Impact of terrestrial weather on the upper atmosphere. *Geophysical Research Letters*, *35*, L09808. https://doi.org/10.1029/2007GL032911

Fuller-Rowell, T. J., & Evans, D. S. (1987). Height-integrated Pedersen and Hall conductivity patterns inferred from the TIROS-NOAA satellite data. *Journal of Geophysical Research*, *92*(A7), 7606–7618. https://doi.org/10.1029/JA092iA07p07606

Garcia, R. R., Marsh, D. R., Kinnison, D. E., Boville, B. A., & Sassi, F. (2007). Simulation of secular trends in the middle atmosphere, 1950–2003. *Journal of Geophysical Research*, *112*, D09301. https://doi.org/10.1029/2006JD007485

Grossmann, K. U., Kaufmann, M., & Gerstner, E. (2000). A global measurement of lower thermosphere atomic oxygen densities. *Geophysical Research Letters*, *27*(9), 1387–1390. https://doi.org/10.1029/2000GL003761

Grossmann, K., & Offermann, D. (1978). Atomic oxygen emission at 63 μm as a cooling mechanism in the thermosphere and ionosphere. *Nature*, *276*, 594–595. https://doi.org/10.1038/276594a0

Gumbel, J. (1997). Rocket-borne optical measurements of minor constituents in the middle atmosphere (Ph.D. thesis), Stockholm University, Department of Meteorology, Stockholm University, Stockholm, Sweden.

Hagan, M. E., & Forbes, J. M. (2002). Migrating and nonmigrating diurnal tides in the middle and upper atmosphere excited by tropospheric latent heat release. *Journal of Geophysical Research*, *107*(D24), 4754. https://doi.org/10.1029/2001JD001236

Hagan, M. E., Maute, A., & Roble, R. G. (2009). Tropospheric tidal effects on the middle and upper atmosphere. *Journal of Geophysical Research*, *114*, A01302. https://doi.org/10.1029/2008JA013637

Hays, P. B., Jones, R. A., & Rees, M. H. (1973). Auroral heating and the composition of the neutral atmosphere. *Planetary and Space Science*, *21*(4), 559–573. https://doi.org/10.1016/0032-0633(73)90070-6

Hedin, A. E. (1983). A revised thermospheric model based on mass spectrometer and incoherent scatter data: MSIS-83. *Journal of Geophysical Research*, *88*(A12), 10,170–10,188. https://doi.org/10.1029/JA088iA12p10170

Hedin, A. E. (1987). MSIS-83 thermospheric model. *Journal of Geophysical Research*, *92*(A5), 4649–4662. https://doi.org/10.1029/JA092iA05p04649

Hedin, A. E. (1991). Extension of the MSIS thermosphere model into the middle and lower atmosphere. *Journal of Geophysical Research*, *96*(A2), 1159–1172. https://doi.org/10.1029/90JA02125

Hodges, R. R. (1969). Eddy diffusion coefficients due to instabilities in internal gravity waves. *Journal of Geophysical Research*, *74*(16), 4087–4090. https://doi.org/10.1029/JA074i016p04087

Humm, D. C., Ogorzalek, B. S., Elko, M. J., Morrison, D., & Paxton, L. J. (1999). Optical calibration of the global ultraviolet imager (GUVI). *Proceedings of SPIE*, *3818*, 3818–3818 –12. https://doi.org/10.1117/12.364144

Humm, D. C., Paxton, L. J., Christensen, A. B., Ogorzalek, B. S., Pardoe, C. T., Meng, C.-I., et al. (1998). Design and performance of the global ultraviolet imager (GUVI). *Proceedings of SPIE*, *3445*, 3445–3445 –11. https://doi.org/10.1117/12.330325

Hysell, D. L., Kelley, M. C., Swartz, W. E., & Woodman, R. F. (1990). Seeding and layering of equatorial spread F by gravity waves. *Journal of Geophysical Research*, *95*(A10), 17,253–17,260. https://doi.org/10.1029/JA095iA10p17253

Immel, T. J., Sagawa, E., England, S. L., Henderson, S. B., Hagan, M. E., Mende, S. B., et al. (2006). Control of equatorial ionospheric morphology by atmospheric tides. *Geophysical Research Letters*, *33*, L15108. https://doi.org/10.1029/2006GL026161

Jin, H., Miyoshi, Y., Fujiwara, H., Shinagawa, H., Terada, K., Terada, N., et al. (2011). Vertical connection from the tropospheric activities to the ionospheric longitudinal structure simulated by a new Earth's whole atmosphere-hionosphere coupled model. *Journal of Geophysical Research*, *116*, A01316. https://doi.org/10.1029/2010JA015925

Johnson, F. S. (1964). Composition changes in the upper atmosphere. In E. Thrane (Ed.), *Electron density distribution in ionosphere and exosphere* (pp. 81–84). North-Holland, Amsterdam.

Johnson, F. S. (1973). Horizontal variations in thermospheric composition. *Reviews of Geophysics*, *11*(3), 741–754. https://doi.org/10.1029/RG011i003p00741

Johnson, F. S., & Gottlieb, B. (1970). Eddy mixing and circulation at ionospheric levels. *Planetary and Space Science*, *18*(12), 1707–1718. https://doi.org/10.1016/0032-0633(70)90004-8

Johnson, F. S., & Gottlieb, B. (1973). Atomic oxygen transport in the thermosphere. *Planetary and Space Science*, *21*(6), 1001–1009. https://doi.org/10.1016/0032-0633(73)90146-3

Jones Jr., M., Emmert, J. T., Drob, D. P., Picone, J. M., & Meier, R. R. (2018). Origins of the thermosphere-ionosphere semiannual oscillation: Reformulating the "thermospheric spoon" mechanism. *Journal of Geophysical Research: Space Physics*, *123*, 931–954. https://doi.org/10.1002/2017JA024861

Jones Jr., M., Emmert, J. T., Drob, D. P., & Siskind, D. E. (2017). Middle atmosphere dynamical sources of the semiannual oscillation in the thermosphere and ionosphere. *Geophysical Research Letters*, *44*, 12–21. https://doi.org/10.1002/2016GL071741

Keating, G. M., & Prior, E. J. (1968). The winter He bulge. *Space Research*, *8*, 982.

Kelly, M. A., Comberiate, J. M., Miller, E. S., & Paxton, L. J. (2014). Progress toward forecasting of space weather effects on UHF SATCOM after operation anaconda. *Space Weather*, *12*, 601–611. https://doi.org/10.1002/2014SW001081

King, G. A. M. (1964). The dissociation of oxygen and high level circulation in the atmosphere. *Journal of the Atmospheric Sciences*, *21*(3), 231–237. https://doi.org/10.1175/1520-0469(1964)0210231:TDOOAH2.0.CO;2

Kirchhoff, V. W. J. H., & Clemesha, B. R. (1983). The atmospheric neutral sodium layer: 2. Diurnal variations. *Journal of Geophysical Research*, *88*(A1), 442–450. https://doi.org/10.1029/JA088iA01p00442

Lin, S.-J. (2004). A "vertically Lagrangian" finite-volume dynamical core for global models. *Monthly Weather Review*, *132*(10), 2293–2307. https://doi.org/10.1175/1520-0493(2004)132<2293:AVLFDC>2.0.CO;2

Lin, F. J., Chance, K. V., & Traub, W. A. (1987). Atomic oxygen in the lower thermosphere. *Journal of Geophysical Research*, *92*(D4), 4325–4336. https://doi.org/10.1029/JD092iD04p04325

Lindzen, R. S. (1981). Turbulence and stress owing to gravity wave and tidal breakdown. *Journal of Geophysical Research*, *86*(C10), 9707–9714. https://doi.org/10.1029/JC086iC10p09707

Liu, H.-L. (2007). On the large wind shear and fast meridional transport above the mesopause. *Geophysical Research Letters*, *34*, L08815. https://doi.org/10.1029/2006GL028789

Liu, H.-L., Bardeen, C. G., Foster, B. T., Lauritzen, P., Liu, J., Lu, G., et al. (2018). Development and validation of the whole atmosphere community climate model with thermosphere and ionosphere extension (WACCM-X 2.0). *Journal of Advances in Modeling Earth Systems*, *10*, 381–402. https://doi.org/10.1002/2017MS001232

Liu, H.-L., Foster, B. T., Hagan, M. E., McInerney, J. M., Maute, A., Qian, L., et al. (2010). Thermosphere extension of the whole atmosphere community climate model. *Journal of Geophysical Research*, *115*, A12302. https://doi.org/10.1029/2010JA015586

Liu, X., Wang, W., Thayer, J. P., Burns, A., Sutton, E., Solomon, S. C., et al. (2014). The winter helium bulge revisited. *Geophysical Research Letters*, *41*, 6603–6609. https://doi.org/10.1002/2014GL061471

Malhotra, G., Ruohoniemi, J. M., Baker, J. B. H., Hibbins, R. E., & McWilliams, K. A. (2016). HF radar observations of a quasi-biennial oscillation in midlatitude mesospheric winds. *Journal of Geophysical Research: Atmospheres*, *121*, 12,677–12,689. https://doi.org/10.1002/2016JD024935

Marsh, D. R., Mills, M. J., Kinnison, D. E., Lamarque, J.-F., Calvo, N., & Polvani, L. M. (2013). Climate change from 1850 to 2005 simulated in CESM1(WACCM). *Journal of Climate*, *26*(19), 7372–7391. https://doi.org/10.1175/JCLI-D-12-00558.1

Mayr, H. G., Harris, I., & Spencer, N. W. (1978). Some properties of upper atmosphere dynamics. *Reviews of Geophysics*, *16*(4), 539–565. https://doi.org/10.1029/RG016i004p00539

Meier, R. R., Picone, J. M., Drob, D., Bishop, J., Emmert, J. T., Lean, J. L., et al. (2014). Remote sensing of earth's limb by TIMED/GUVI: Retrieval of thermospheric composition and temperature. *Earth and Space Science*, *2*, 1–37. https://doi.org/10.1002/2014EA000035

Mlynczak, M. G. (1996). Energetics of the middle atmosphere: Theory and observation requirements. *Advances in Space Research*, *17*(11), 117–126. https://doi.org/10.1016/0273-1177(95)00739-2

Mlynczak, M. G. (1997). Energetics of the mesosphere and lower thermosphere and the SABER experiment. *Advances in Space Research*, *20*(6), 1177–1183. (Coupling and Energetics in the Stratosphere-Mesosphere-Thermosphere-Ionosphere System) https://doi.org/10.1016/S0273-1177(97)00769-2

Mlynczak, M. G., Hunt, L. A., Mast, J. C., Thomas Marshall, B., Russell III, J. M., Smith, A. K., et al. (2013). Atomic oxygen in the mesosphere and lower thermosphere derived from SABER: Algorithm theoretical basis and measurement uncertainty. *Journal of Geophysical Research: Atmospheres*, *118*, 5724–5735. https://doi.org/10.1002/jgrd.50401

Mlynczak, M. G., Hunt, L. A., Russell III, J. M., & Marshall, B. T. (2018). Updated SABER night atomic oxygen and implications for SABER ozone and atomic hydrogen. *Geophysical Research Letters*, *45*, 5735–5741. https://doi.org/10.1029/2018GL077377

Mlynczak, M. G., Martin-Torres, F. J., Johnson, D. G., Kratz, D. P., Traub, W. A., & Jucks, K. (2004). Observations of the O(3P) fine structure line at 63μm in the upper mesosphere and lower thermosphere. *Journal of Geophysical Research*, *109*, A12306. https://doi.org/10.1029/2004JA010595

Offermann, D. (1974). Composition variations in the lower thermosphere. *Journal of Geophysical Research*, *79*(28), 4281–4293. https://doi.org/10.1029/JA079i028p04281

Paxton, L. J., Christensen, A. B., Humm, D. C., Ogorzalek, B. S., Pardoe, C. T., Morrison, D., et al. (1999). Global ultraviolet imager (GUVI): Measuring composition and energy inputs for the NASA Thermosphere Ionosphere Mesosphere Energetics and Dynamics (TIMED) mission. In A. M. Larar (Ed.), *Optical spectroscopic techniques and instrumentation for atmospheric and space research III* (Vol. 3756, pp. 265–276). Bellingham, Wash: International Society for Optics and Photonics. https://doi.org/10.1117/12.366380

Paxton, L. J., Christensen, A. B., Morrison, D., Wolven, B., Kil, H., Zhang, Y., et al. (2004). GUVI: A hyperspectral imager for geospace. In C. A. Nardell, P. G. Lucey, J.-H. Yee, & J. B. Garvin (Eds.), *Instruments, science, and methods for geospace and planetary remote sensing* (Vol. 5660, pp. 228–240). Bellingham, Wash: International Society for Optics and Photonics. https://doi.org/10.1117/12.579171

Perlongo, N. J., Ridley, A. J., Cnossen, I., & Wu, C. (2018). A year-long comparison of GPS TEC and global ionosphere-thermosphere models. *Journal of Geophysical Research: Space Physics*, *123*, 1410–1428. https://doi.org/10.1002/2017JA024411

Picone, J. M., Hedin, A. E., Drob, D. P., & Aikin, A. C. (2002). NRLMSISE-00 empirical model of the atmosphere: Statistical comparisons and scientific issues. *Journal of Geophysical Research*, *107*(A12), 1468. https://doi.org/10.1029/2002JA009430

Pilinski, M. D., & Crowley, G. (2015). Seasonal variability in global eddy diffusion and the effect on neutral density. *Journal of Geophysical Research: Space Physics*, *120*, 3097–3117. https://doi.org/10.1002/2015JA021084

Prakash, S. (1999). Production of electric field perturbations by gravity wave winds in the *E* region suitable for initiating equatorial spread F. *Journal of Geophysical Research*, *104*(A5), 10,051–10,069. https://doi.org/10.1029/1999JA900028

Qian, L., Burns, A. G., Emery, B. A., Foster, B., Lu, G., Maute, A., et al. (2014). The NCAR TIE-GCM. In J. Huba, R. Schunk, & G. Khazanov (Eds.), *Modeling the ionosphere-thermosphere system, Geophysical Monograph Series* (pp. 73–83). Washington, DC: John Wiley & Sons. https://doi.org/10.1002/9781118704417.ch7

Qian, L., Burns, A. G., Solomon, S. S., Smith, A. K., McInerney, J. M., Hunt, L. A., et al. (2018). Temporal variability of atomic hydrogen from the mesopause to the upper thermosphere. *Journal of Geophysical Research: Space Physics*, *123*, 1006–1017. https://doi.org/10.1002/2017JA024998

Qian, L., Burns, A., & Yue, J. (2017). Evidence of the lower thermospheric winter-to-summer circulation from SABER CO_2 observations. *Geophysical Research Letters*, *44*, 10,100–10,107. https://doi.org/10.1002/2017GL075643

Qian, L., Solomon, S. C., & Kane, T. J. (2009). Seasonal variation of thermospheric density and composition. *Journal of Geophysical Research*, *114*, A01312. https://doi.org/10.1029/2008JA013643

Qian, L., & Yue, J. (2017). Impact of the lower thermospheric winter-to-summer residual circulation on thermospheric composition. *Geophysical Research Letters*, *44*, 3971–3979. https://doi.org/10.1002/2017GL073361

Reber, C. A., Cooley, J. E., & Harpold, D. N. (1968). Upper atmosphere hydrogen and helium measurements from the explorer 32 satellite. *Space Research*, *8*, 993.

Reber, C. A., & Hays, P. B. (1973). Thermospheric wind effects on the distribution of helium and argon in the Earth's upper atmosphere. *Journal of Geophysical Research*, *78*(16), 2977–2991. https://doi.org/10.1029/JA078i016p02977

Rezac, L., Jian, Y., Yue, J., Russell III, J. M., Kutepov, A., Garcia, R., et al. (2015). Validation of the global distribution of CO_2 volume mixing ratio in the mesosphere and lower thermosphere from SABER. *Journal of Geophysical Research: Atmospheres*, *120*, 12,067–12,081. https://doi.org/10.1002/2015JD023955

Richmond, A. D., Ridley, E. C., & Roble, R. G. (1992). A thermosphere/ionosphere general circulation model with coupled electrodynamics. *Geophysical Research Letters*, *19*(6), 601–604. https://doi.org/10.1029/92GL00401

Ridley, A. J., Deng, Y., & Tóth, G. (2006). The global ionosphere-thermosphere model. *Journal of Atmospheric and Solar-Terrestrial Physics*, *68*(8), 839–864. https://doi.org/10.1016/j.jastp.2006.01.008

Rienecker, M. M., Suarez, M. J., Gelaro, R., Todling, R., Bacmeister, J., Liu, E., et al. (2011). MERRA: NASA's modern-era retrospective analysis for research and applications. *Journal of Climate*, *24*(14), 3624–3648. https://doi.org/10.1175/JCLI-D-11-00015.1

Rishbeth, H. (1998). How the thermospheric circulation affects the ionospheric F2-layer. *Journal of Atmospheric and Solar-Terrestrial Physics*, *60*(14), 1385–1402. https://doi.org/10.1016/S1364-6826(98)00062-5

Roble, R. G. (2013). On the feasibility of developing a global atmospheric model extending from the ground to the exosphere. In D. E. Siskind, S. D. Eckermann, & M. E. Summers (Eds.), *Atmospheric science across the stratopause, Geophysical Monograph Series* (pp. 53–67). Washington, DC: American Geophysical Union (AGU). https://doi.org/10.1029/GM123p0053

Rottger, J. (1973). Wave-like structures of large-scale equatorial spread-F irregularities. *Journal of Atmospheric and Terrestrial Physics*, *35*(6), 1195–1206. https://doi.org/10.1016/0021-9169(73)90016-0

Russell, J. III, Mlynczak, M., Gordley, L., Tansock, J., & Esplin, R. (1999). Overview of the SABER experiment and preliminary calibration results. In A. M. Larar (Ed.), *Optical spectroscopic techniques and instrumentation for atmospheric and space research III* (Vol. *3756*, pp. 277–288). Bellingham, Wash: International Society for Optics and Photonics. https://doi.org/10.1117/12.366382

Russell, J. P., Lowe, R. P., & Ward, W. E. (2004). Atomic oxygen annual and semi-annual variations in the mesopause region for mid and equatorial latitudes. *Journal of Atmospheric and Solar-Terrestrial Physics*, *66*(6), 451–461. Retrieved from http://www.sciencedirect.com/science/article/pii/S1364682604000124 (Dynamics and Chemistry of the MLT Region - PSMOS 2002 International Symposium). https://doi.org/10.1016/j.jastp.2004.01.004

Salinas, C. C. J. H., Chang, L. C., Liang, M. C., Yue, J., Russell, J., & Mlynczak, M. (2016). Impacts of SABER CO_2 based eddy diffusion coefficients in the lower thermosphere on the ionosphere/thermosphere. *Journal of Geophysical Research: Space Physics*, *121*, 12,080–12,092. https://doi.org/10.1002/2016JA023161

Sasi, M. N., & Vijayan, L. (2001). Turbulence characteristics in the tropical mesosphere as obtained by MST radar at Gadanki (13.5°N, 79.2°E). *Annales Geophysicae*, *19*(8), 1019–1025. https://doi.org/10.5194/angeo-19-1019-2001

Schunk, R., & Nagy, A. (2009). *Ionospheres: Physics, plasma physics, and chemistry, Cambridge Atmospheric and Space Science Series* (2nd ed., pp. 269–311). Cambridge, United Kingdom: Cambridge University Press. https://doi.org/10.1017/CBO9780511635342

Sheese, P. E., McDade, I. C., Gattinger, R. L., & Llewellyn, E. J. (2011). Atomic oxygen densities retrieved from optical spectrograph and infrared imaging system observations of O_2 A-band airglow emission in the mesosphere and lower thermosphere. *Journal of Geophysical Research*, *116*, D01303. https://doi.org/10.1029/2010JD014640

Shimazaki, T. (1965). On the continuity equation for electron density in the ionosphere. *Journal of Atmospheric and Terrestrial Physics*, *27*(5), 593–604. https://doi.org/10.1016/0021-9169(65)90127-3

Shimazaki, T. (1966). Nighttime variations of *F*-region electron density profiles at Puerto Rico: 2. An attempt to separate the effects of temperature variation and drift velocity. *Journal of Geophysical Research*, *71*(13), 3177–3190. https://doi.org/10.1029/JZ071i013p03177

Shimazaki, T. (1967). Dynamic effects on atomic and molecular oxygen density distributions in the upper atmosphere: A numerical solution to equations of motion and continuity. *Journal of Atmospheric and Terrestrial Physics*, *29*(6), 723–747. https://doi.org/10.1016/0021‐9169(67)90216-4

Shimazaki, S. (1968). Dynamic effects on height distributions of neutral constituents in the Earth's upper atmosphere: A calculation of atmospheric model between 70 km and 500 km. *Journal of Atmospheric and Terrestrial Physics*, *30*(7), 1279–1292. https://doi.org/10.1016/S0021-9169(68)91107-0

Siskind, D. E., Drob, D. P., Dymond, K. F., & McCormack, J. P. (2014). Simulations of the effects of vertical transport on the thermosphere and ionosphere using two coupled models. *Journal of Geophysical Research: Space Physics*, *119*, 1172–1185. https://doi.org/10.1002/2013JA019116

Smith, A. K., Garcia, R. R., Marsh, D. R., & Richter, J. H. (2011). WACCM simulations of the mean circulation and trace species transport in the winter mesosphere. *Journal of Geophysical Research*, *116*, D20115. https://doi.org/10.1029/2011JD016083

Smith, A. K., Harvey, V. L., Mlynczak, M. G., Funke, B., García-Comas, M., Hervig, M., et al. (2013). Satellite observations of ozone in the upper mesosphere. *Journal of Geophysical Research: Atmospheres*, *118*, 5803–5821. https://doi.org/10.1002/jgrd.50445

Smith, A. K., Marsh, D. R., Mlynczak, M. G., & Mast, J. C. (2010). Temporal variations of atomic oxygen in the upper mesosphere from SABER. *Journal of Geophysical Research*, *115*, D18309. https://doi.org/10.1029/2009JD013434

Sutton, E. K. (2016). Interhemispheric transport of light neutral species in the thermosphere. *Geophysical Research Letters*, *43*, 12,325–12,332. https://doi.org/10.1002/2016GL071679

von Zahn, U. (1967). Mass spectrometric measurements of atomic oxygen in the upper atmosphere: A critical review. *Journal of Geophysical Research*, *72*(23), 5933–5937. https://doi.org/10.1029/JZ072i023p05933

Walker, J. C. G. (1965). Analytic representation of upper atmosphere densities based on Jacchia's static diffusion models. *Journal of the Atmospheric Sciences*, *22*(4), 462–463. https://doi.org/10.1175/1520-0469(1965)022<0462:AROUAD>2.0.CO;2

Weimer, D. R. (2005). Improved ionospheric electrodynamic models and application to calculating joule heating rates. *Journal of Geophysical Research*, *110*, A05306. https://doi.org/10.1029/2004JA010884

Weimer, D. R., Mlynczak, M. G., Emmert, J. T., Doornbos, E., Sutton, E. K., & Hunt, L. A. (2018). Correlations between the thermosphere's semiannual density variations and infrared emissions measured with the SABER instrument. *Journal of Geophysical Research: Space Physics*, *123*, 8850–8864. https://doi.org/10.1029/2018JA025668

Wu, Q., Ortland, D. A., Foster, B., & Roble, R. G. (2012). Simulation of nonmigrating tide influences on the thermosphere and ionosphere with a TIMED data driven TIEGCM. *Journal of Atmospheric and Solar-Terrestrial Physics*, *90-91*, 61–67. (Recent Progress in the Vertical Coupling in the Atmosphere-Ionosphere System). https://doi.org/10.1016/j.jastp.2012.02.009

Wu, D. L., Yee, J.-H., Schlecht, E., Mehdi, I., Siles, J., & Drouin, B. J. (2016). THz limb sounder (TLS) for lower thermospheric wind, oxygen density, and temperature. *Journal of Geophysical Research: Space Physics*, *121*, 7301–7315. https://doi.org/10.1002/2015JA022314

Yamazaki, Y., & Richmond, A. D. (2013). A theory of ionospheric response to upward-propagating tides: Electrodynamic effects and tidal mixing effects. *Journal of Geophysical Research: Space Physics*, *118*, 5891–5905. https://doi.org/10.1002/jgra.50487

Yee, J. H. (2003). TIMED mission science overview. *John Hopkins APL Technical Digest*, *24*(2), 136–141 Apr–Jun.

Yue, J., Jian, Y., Wang, W., Meier, R. R., Burns, A., Qian, L., et al. (2019). Annual and semiannual oscillations of thermospheric composition in TIMED/GUVI limb measurements. *Journal of Geophysical Research: Space Physics*, *124*, 3067–3082. https://doi.org/10.1029/2019JA026544

Zhang, X., Forbes, J. M., & Hagan, M. E. (2010a). Longitudinal variation of tides in the MLT region: 2. Relative effects of solar radiative and latent heating. *Journal of Geophysical Research*, *115*, A06317. https://doi.org/10.1029/2009JA014898

Zhang, X., Forbes, J. M., & Hagan, M. E. (2010b). Longitudinal variation of tides in the MLT region: 1. Tides driven by tropospheric net radiative heating. *Journal of Geophysical Research*, *115*, A06316. https://doi.org/10.1029/2009JA014897

Zhang, Y., Paxton, L. J., Morrison, D., Marsh, D., & Kil, H. (2014). Storm-time behaviors of O/N_2 and NO variations. *Journal of Atmospheric and Solar-Terrestrial Physics*, *114*, 42–49. https://doi.org/10.1016/j.jastp.2014.04.003

Zhang, Y., Paxton, L. J., Morrison, D., Wolven, B., Kil, H., Meng, C. I., et al. (2004). O/N_2 changes during 1–4 october 2002 storms: IMAGE SI-13 and TIMED/GUVI observations. *Journal of Geophysical Research*, *109*, A10308. https://doi.org/10.1029/2004JA010441